

SKYSURF-4: Panchromatic Full Sky Surface Brightness Measurement Methods and Results

ROSALIA O'BRIEN,¹ TIMOTHY CARLETON,¹ ROGIER A. WINDHORST,¹ ROLF A. JANSEN,¹ DELONDRAE CARTER,¹ SCOTT TOMPKINS,² SARAH CADDY,³ SETH H. COHEN,¹ HALEY ABATE,¹ RICHARD G. ARENDT,⁴ JESSICA BERKHEIMER,¹ ANNALISA CALAMIDA,⁵ STEFANO CASERTANO,⁵ SIMON P. DRIVER,⁶ CONNOR GELB,¹ ZAK GOISMAN,¹ NORMAN GROGIN,⁵ DANIEL HENNINGSEN,¹ ISABELA HUCKABEE,¹ SCOTT J. KENYON,⁷ ANTON M. KOEKEMOER,⁵ DARBY KRAMER,¹ JOHN MACKENTY,⁵ AARON ROBOTHAM,⁶ AND STEVEN SHERMAN¹

¹*School of Earth and Space Exploration, Arizona State University, Tempe, AZ 85287-1404, USA*

²*The University of Western Australia, M468, 35 Stirling Highway, Crawley, WA 6009, Australia*

³*Macquarie University, Sydney, NSW 2109, Australia*

⁴*UMBC/CRESST2, NASA Goddard Space Flight Center, Greenbelt, MD 20771, USA*

⁵*Space Telescope Science Institute, 3700 San Martin Drive, Baltimore, MD 21210, USA*

⁶*International Centre for Radio Astronomy Research (ICRAR) and the International Space Centre (ISC), The University of Western Australia, M468, 35 Stirling Highway, Crawley, WA 6009, Australia*

⁷*Smithsonian Astrophysical Observatory, 60 Garden Street, Cambridge, MA 02138, USA*

ABSTRACT

The diffuse, unresolved sky provides most of the photons that the Hubble Space Telescope (HST) receives, yet remains poorly understood. HST Archival Legacy program SKYSURF aims to measure the 0.2–1.7 μm sky surface brightness (sky-SB) from over 200,000 HST images. We describe two sky-SB measurement algorithms designed for SKYSURF (the Percentile-clip and ProFound Median methods), that are able to recover the input sky-SB from simulated images to within 1% uncertainty, and present measurements estimated using each algorithm on the entire SKYSURF database. Comparing our sky-SB spectral energy distribution to measurements from the literature shows general agreements, but highlights that models of Zodiacal Light at HST wavelengths are likely incomplete. Our SKYSURF spectral energy distribution also reveals a dependence on Sun Angle, indicating non-isotropic scattering of Solar photons. Finally, we update Diffuse Light limits for F125W, F140W, and F160W based on the methods from Carleton et al. (2022). The Diffuse Light limits for both sky-SB measurements algorithms are in good agreement, ranging from 0.006 MJy sr⁻¹ (14 nW m⁻² sr⁻¹) to 0.015 MJy sr⁻¹ (32 nW m⁻² sr⁻¹). These estimates provide the most stringent all-sky constraints to date in this wavelength range. SKYSURF sky-SB measurements are made public on the official SKYSURF website and will be used to constrain Extragalactic Background Light in future papers.

Keywords: Instruments: Hubble Space Telescope — Solar System: Zodiacal Foreground — Cosmology: Extragalactic Background Light

1. INTRODUCTION

The diffuse sky is an extended source of light present in all astronomical images, and is responsible for more than 95% of all photons the Hubble Space Telescope (HST) receives at wavelengths between 0.6 μm and 1.25 μm . (Windhorst et al. 2022). The measured sky surface brightness (sky-SB) in HST images is a combination of Zodiacal Light (ZL), Diffuse Galactic Light (DGL),

and Extragalactic Background Light (EBL). ZL is the brightest component of the sky-SB, and is a result of sunlight scattering off interplanetary dust (Hulst 1947; Leinert et al. 1998; Kelsall et al. 1998; Sano et al. 2020; Korngut et al. 2022). Scattered light by dust and gas in the interstellar medium, as well as unresolved faint stars, causes DGL (e.g., Arendt et al. 1998; Schlegel et al. 1998; Brandt & Draine 2011). Finally, EBL consists of *all* far-UV to far-IR extragalactic photons, including light from stars, AGN, and dust attenuation/ re-radiation (e.g., Andrews et al. 2017; Hill et al. 2018; Driver 2021). While many projects have studied the various sky-SB

components, each component is understood at varying levels of certainty.

Uncertainties in ZL make studies of the other components of the sky-SB, most notably EBL, difficult. We exist inside the Interplanetary Dust Cloud (IPD), making ZL especially difficult to constrain. Kelsall et al. (1998) was the first Zodiacal model to utilize NASA’s Cosmic Background Explorer (COBE) Diffuse Infrared Background Experiment (DIRBE), which spans $1.25\ \mu\text{m}$ to $240\ \mu\text{m}$ and characterizes the annual modulation of ZL emission to produce a three-dimensional model. COBE/DIRBE ZL emission maps have excellent relative accuracies of 1% to 2% (Leinert et al. 1998), but are limited to Sun Angles of $94\ \text{deg} \pm 30\ \text{deg}$ (Sun Angle refers to the angle between the observation and the Sun, as shown in Figure 2 of Caddy et al. 2022). This range of Sun Angles would allow the detection of any nearby isotropic/ spherically symmetric component of the IPD (Hauser et al. 1998), but potentially miss a more distant component (e.g., Sano et al. 2020). Wright (1998) used COBE/DIRBE data with the condition that the lowest $25\ \mu\text{m}$ sky-SB at high ecliptic latitudes is only ZL, such that subtracting the ZL model from in this regime yields a sky-SB level of zero. This condition means that the Wright model includes flux from any isotropic component that the Kelsall model might not account for, but also runs the risk of attributing some EBL to ZL. Although these robust models of ZL exist at infrared wavelengths, there is limited data below $1.25\ \mu\text{m}$ to create similar models. Leinert et al. (1998) introduced a parametric ZL model that reaches HST wavelengths, and is a function of viewing direction (including Sun Angle), wavelength, heliocentric distance, and position of the observer relative to the plane of interplanetary dust. This model assumes ZL to follow a reddened solar spectrum. Aldering (2001) modified the Leinert model based on observations at the North Ecliptic Pole.

The DGL is relatively well understood, with several models existing at varying wavelength ranges. In the Near-to-Far-IR, Arendt et al. (1998) present a $1.25\ \mu\text{m} - 240\ \mu\text{m}$ model of DGL using COBE/DIRBE maps, while Schlegel et al. (1998) presents a full-sky $100\ \mu\text{m}$ map (where ZL is minimal) based on COBE/DIRBE data and Infrared Astronomy Satellite (IRAS) ISSA maps. In the optical, Brandt & Draine (2011) uses blank sky spectra from the Sloan Digital Sky Survey (SDSS) to attain optical spectra of DGL.

EBL might be the least understood component of the sky-SB (e.g., Hill et al. 2018; Driver 2021), which is unfortunate because it offers unique constraints on galaxy formation and evolution (e.g., Domínguez et al. 2011; Somerville et al. 2012), as it as probes star formation,

AGN activity, and dust properties over cosmic time (e.g., Andrews et al. 2017). However, due to uncertainties in ZL at HST wavelengths, EBL measurements in this regime are controversial. Direct EBL measurements (e.g., Hauser et al. 1998; Dwek & Arendt 1999; Cambresy et al. 2001; Matsumoto et al. 2005; Bernstein 2007; Dole, H. et al. 2006; Matsuura et al. 2017; Lauer et al. 2021) require robust subtraction of foregrounds such as ZL and DGL, and absolute calibration of the instrument. Some experiments use unique methods to better account for ZL emission. The CIBER experiment (Matsuura et al. 2017; Korngut et al. 2022) use Ca absorption features to better estimate ZL, while the Pioneer and New Horizons missions (Matsumoto et al. 2018; Lauer et al. 2021; Lauer et al. 2022) leave the inner Solar System entirely to heliocentric distances where ZL emission is reduced.

In contrast, an estimate of EBL can be obtained by integrating the total flux from galaxy counts that are extrapolated to the faint end (Driver et al. 2016; Koushan et al. 2021). Direct measurements of EBL as compared to these models derived from deep galaxy counts provides the basis for EBL studies, yet reveals an interesting disparity. This comparison yields $3-5\times$ more EBL at optical wavelengths than we would expect based on galaxy counts alone (see Driver et al. 2016; Windhorst et al. 2022). We refer to this unaccounted-for EBL signal as Diffuse Light (DL).

There are many potential sources for DL, ranging from an incomplete understanding of our universe (missing galaxies, extended outskirts of galaxies, intrahalo light, Reionization), our local universe (underestimated ZL or DGL models), and our instruments (telescope glow, Earthshine), as well as more extreme sources such as dark matter particles or black holes. We summarize them here:

1. Undetected galaxies: There could be more unresolved galaxies than models predict or existing observations identify (Conselice et al. 2016; Lauer et al. 2021). Integrated galaxy light (IGL) predictions of EBL (Driver et al. 2016) assume that the number of faint and unresolved galaxies will follow the trend that resolved galaxies imply. If there are more faint galaxies in the universe than we can observe, IGL predictions will be underestimated. However, Kramer et al. (2022) place strong constraints on the contribution to DL.
2. Extended profiles of galaxies: The extended profiles of galaxies (e.g., Li et al. 2022; Gilhuly et al. 2022) could contaminate sky-SB measurements. Studies (Ashcraft et al. 2018, 2022; Cheng et al. 2021) have found that no more than 10–20% of light is missed

in the outskirts of galaxies from traditional source finding techniques. Therefore, this cannot fully explain the total measured DL levels, but may contribute to some of it.

3. **Intrahalo light:** Intrahalo light is diffuse light from stars tidally stripped from their hosts (Zemcov et al. 2014). Rich clusters could contain 10–50% of their total luminosity in diffuse intrahalo light (Bernstein et al. 1995; Rudick et al. 2011; Mihos 2019), which could be picked up in sky-SB measurements. Intrahalo light can only affect optical measurements because UV flux destroys any dust particles (which would emit in the IR) in the intracluster medium (Driver et al. 2016). Since we do not see similar discrepancies in EBL versus IGL measurements in the far-IR, intrahalo light remains a candidate for DL.
4. **The Epoch of Reionization:** This era refers to a period where the first stars and galaxies were ionizing the universe around them. Some studies suggest that these stars should contribute to EBL at infrared wavelengths (Santos et al. 2002; Cooray et al. 2004; Kashlinsky et al. 2004; Matsumoto et al. 2011), but the flux from this era is likely not higher than $\sim 2 \text{ nW m}^{-2} \text{ sr}^{-1}$ at $1 \mu\text{m}$ (Madau & Silk 2005).
5. **Telescope Glow:** HST is known to emit radiation in the Near-IR that can contribute to the sky-SB at these wavelengths (SKYSURF-2).
6. **Incomplete ZL or DGL models:** If models of ZL or DGL are underestimated from their true values, this could cause direct EBL measurements to appear higher than they truly are. Some studies (Kawara et al. 2017; Korngut et al. 2021) find evidence of an isotropic ZL component that is missed in conventional models.
7. **Dark matter (DM) particles,** such as self-annihilating DM particles powering a new type of star (Maurer et al. 2012), or DM-photon decays (Gong et al. 2016)
8. **Accreting direct-collapse black holes at high redshift** (Yue et al. 2013).

The Hubble Space Telescope’s (HST’s) capability as an ultra-sensitive, absolute photometer provides us with the necessary sensitivity to study the sky-SB and constrain the amount of EBL and DL in the universe to high precision. SKYSURF is an HST archival program to measure the 0.2–1.7 μm sky-SB from over 200,000 HST

images spanning 4 cameras, providing unprecedented constraints on ZL, DGL, and EBL. Windhorst et al. (2022, hereafter SKYSURF-1) summarizes Project SKYSURF, and Carleton et al. (2022, hereafter SKYSURF-2) provides upper limits to DL for HST’s three reddest filters. To summarize here, SKYSURF has two main project goals. The first consists of robust sky-SB measurements across our entire SKYSURF database. This involves creating and implementing algorithms that can measure the sky-SB level in any HST image without including flux from discrete sources. The second project goal is to attain accurate star and galaxy counts using the entire SKYSURF database. With sky-SB measurements and discrete galaxy counts in hand, we can measure an EBL signal by subtracting ZL and DGL from the total sky-SB signal.

In this report, we present our methods and results for the first SKYSURF goal: panchromatic sky-SB measurements of over 200,000 HST images. In Section 2, we explain our SKYSURF database in detail. Section 3 then explains our methods for estimating the sky-SB from any HST image. Section 4 describes our sources of uncertainty. Section 5 describes how we choose reliable sky-SB measurements. In Section 6, we show our sky-SB results across our entire database, including a SKYSURF spectral energy distribution (SED) of the sky-SB at HST wavelengths. We present updated SKYSURF DL limits in Section 7. Finally, Section 8 explains SKYSURF data products that are released to the public.

2. SKYSURF DATABASE

Our SKYSURF database includes more than 200,000 usable HST observations, as summarized in SKYSURF-1. In this paper, we focus on data taken with HST’s newest cameras: the Wide Field Camera 3 (WFC3) and the Advanced Camera for Surveys (ACS). For comparison, we also measure sky-SB levels for the Wide Field and Planetary Camera 2 (WFPC2; in prep), the predecessor to WFC3. We utilize the UV-Optical (UVIS) and Infrared (IR) channels of WFC3, as well as the Wide Field Channel (WFC) of ACS.

With such a large database, we expect a huge range of target types (e.g., gas clouds, star clusters, blank fields, resolved galaxies, etc) and exposure types (e.g., short and long imaging exposures, grism finder images or DASH observations). For the purpose of the SKYSURF program, certain exposures are not useful and were excluded. We filtered out very short exposures, exposures taken through narrowband filters, quad filters, polarizers, and dispersive elements. Exposure times less than 200 seconds are not used because the read noise is too high for statistically reliable measurements of the sky-SB. In

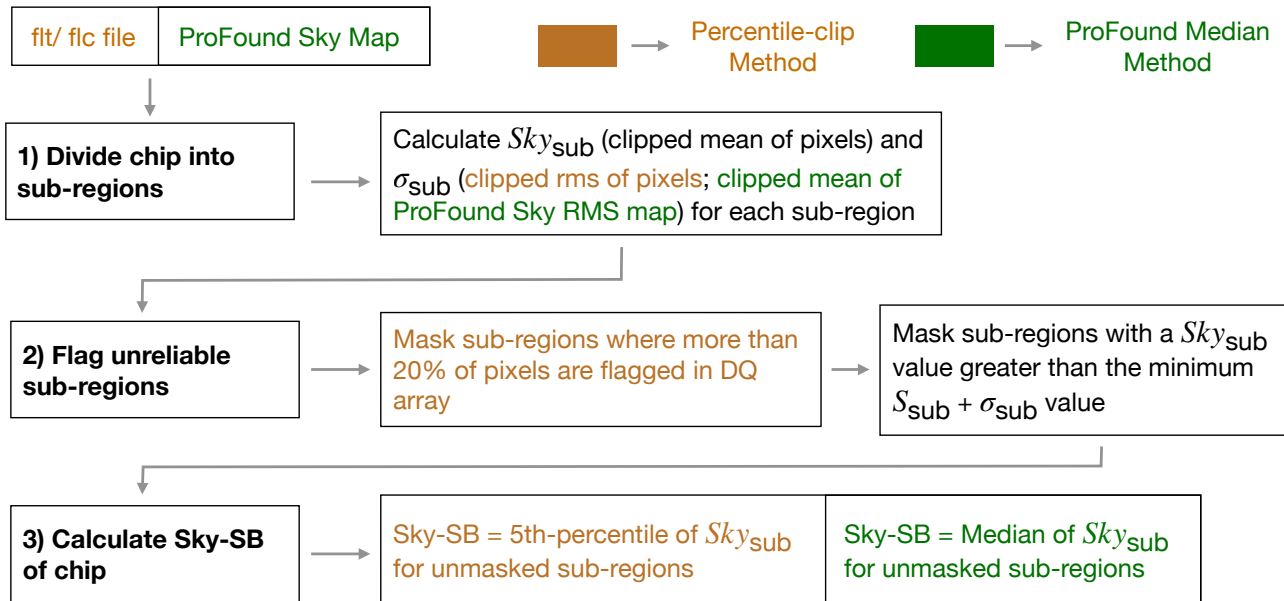


Figure 1. Flowchart of the Per-clip and Pro-med pipelines. These methods estimate the sky-SB for any HST image, as explained in Section 3. The Per-clip method is shown in orange (always on the left-hand side) and the Pro-med method is shown in green (right-hand side). Black text means it is relevant for both methods. Note the DQ masking in step 2 only applies to the Per-clip method.

addition, because the sky-SB is so low in images with short exposure times, errors associated with post-flash (Biretta & Baggett 2013) become a significant issue. We also do not utilize images taken in a subarrayed mode, where only a specific portion of the detector is used. Finally, ACS includes linear ramp (full WFC coverage at continuously varying narrow bandwidth) and polarizing filters, both of which are not used for SKYSURF. Overall, our sky-SB measurement algorithms (Section 3) are optimized for intermediate to long exposures through HST’s sensitive wider band filters.

The standard WFC3 and ACS pipelines create two main types of bias-subtracted, dark-frame subtracted, flat-fielded images: `f1t` and `f1c` files, where the latter includes Charge Transfer Efficiency (CTE) corrections. Since CTE trails do not affect non-destructively read Near-IR detectors, we use the `f1t` files for WFC3/IR. We measure sky-SB levels on 139,078 WFC3 and ACS images. This includes 41,896 WFC3/IR `f1t` images, 21,805 WFC3/UVIS `f1c` images, and 75,377 ACS/WFC `f1c` images. Within this sample, there are 4538 unique proposals and 22,196 unique target names. We report sky-SB measurements through 6 WFC3/IR, 14 WFC3/UVIS, and 8 ACS/WFC filters.

3. SKY-SB MEASUREMENT ALGORITHMS

As shown in SKYSURF-1 and Appendix B here, we tested various algorithms using simulated images, and chose two methods to perform our sky-SB estimations.

We simulated WFC3/IR F125W images with realistic galaxy and star counts, with exposure times ranging from 50 to 1302 seconds, sky-SB levels ranging from 0.22 to 3.14 electrons per second, and sky gradients ranging from 0% to 20% across the field of view. Appendix A describes the creation of these simulated images in detail. We choose the two best algorithms which are able to retrieve the known input sky-SB from the simulated images in the presence of sky gradients.

Final sky-SB measurements were performed using the Percentile-clip method (Per-clip method) and the ProFound Median method (Pro-med method). In this section, we explain the Per-clip and Pro-med methods in detail. A flowchart showing both pipelines is given in Figure 1. Both methods were tested on the realistic HST F125W simulated images (Appendix A) and are found to be able to retrieve the input sky-SB to within 1% (see Figure 12).

3.1. Percentile-clip Method

Many SKYSURF images contain light from the extended profiles of galaxies (Ashcraft et al. 2018), the extended point-spread functions (PSFs) of stars (Borlaff et al. 2019), thermal foregrounds (SKYSURF-2), sky gradients when observations are pushed too close to Earth’s limb or taken at relatively small Moon or Sun angles (Caddy et al. 2022), faint galaxies that are hidden in the noise, and Diffuse Light. We do not want these specific sources of flux to contaminate our sky-SB measurements,

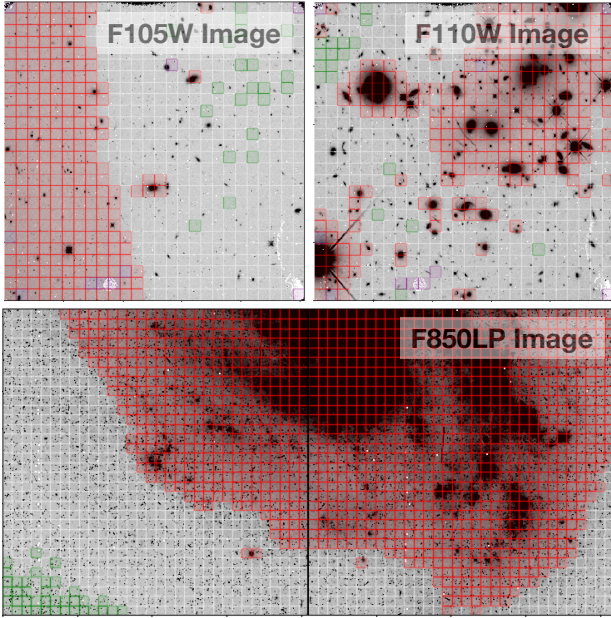


Figure 2. SKYSURF inspection figures for the Per-clip method. We show how this algorithm is able to mask certain areas of an image while estimating the sky-SB. These figures are used to manually flag images where a guide star was lost, with satellite trails, or with other image artifacts (e.g., optical ghosts). Red regions denote sub-regions where our algorithm detects an object. Purple regions denote regions where more than 30% of the pixels are flagged in the DQ array. Green regions show the darkest 5% of remaining sub-regions.

as we want to measure the ZL+DGL+EBL signal. Therefore, the value closest to the true ZL+DGL+EBL signal will be the darkest area in an image (the HST field of view is small enough that gradients in an image due to gradients in ZL emission are negligible). The Per-clip method utilizes this principle.

The Per-clip method follows three steps: 1) Divide each HST chip into sub-regions and calculate sky levels for each sub-region, 2) Flag sub-regions with unreliable sky measurements, then 3) Choose the sub-regions with the lowest sky-SB levels to determine the true sky-SB of the image. We begin by masking all pixels flagged (flag > 0) in the Data Quality (DQ) array associated with the science image (SCI) in each `f1t` or `f1c` file. DQ flags indicate pixels that can be unreliable, including pixels contaminated with cosmic rays, saturated pixels, or known bad detector pixels. Pixels that are affected by persistence are not flagged here, but we explore their effect in Section 4. Next, we divide each image into sub-regions. WFC3/IR is the simplest case, where all images in our sample are 1014×1014 pixels. We split each WFC3/IR image into 39×39 pixel regions, for a total of $26 \times 26 = 676$ sub-regions per image. For WFC3/UVIS,

a full-frame detector image has dimensions of 2051×4096 pixels. For this case, we make each sub-region 64×64 pixels, where remaining pixels will be added to the sub-region on the top-most and right-most sub-regions. For ACS/WFC, the detector has dimensions 2048×4096 , and we follow the same binning technique as for WFC3/UVIS. Both WFC3/UVIS and ACS/WFC images include two CCD detectors (stored as separate science extensions), and we perform sky-SB measurements on each detector independently.

Next, we calculate a sky level (S_{sub}) and sky rms level (σ_{sub}) for each sub-region, each of which are in native pixel units: electrons per second for WFC3/IR and electrons for WFC3/UVIS and ACS/WFC. We first mask all outlier pixels within a single sub-region that are clearly not part of the background (we use boundary values of -126.5 and 895.5 , in native `f1t/f1c` pixel units). The mean (S'_{sub}) and standard deviation (σ'_{sub}) of the remaining pixels are then recorded. We then mask pixels which have a value less than $S'_{\text{sub}} - 5 \times (\sigma'_{\text{sub}})$ or more than $S'_{\text{sub}} + 3 \times (\sigma'_{\text{sub}})$. We are more stringent with the upper cutoff since most sources of sky-SB contamination are brighter than the true sky-SB. New values of S'_{sub} and σ'_{sub} are calculated for the remaining pixels. This process is repeated until there are no outlier pixels remaining. The median (standard deviation) value of the last iteration is saved as the S_{sub} (σ_{sub}) for that sub-region.

Sub-regions are masked based on two criteria. First, we mask sub-regions where more than 20% of the pixels are masked due to DQ flags. Secondly, we compare each S_{sub} in a single sub-region to all the other S_{sub} values in a single image. If a S_{sub} value for a sub-region is greater than the minimum $S_{\text{sub}} + \sigma_{\text{sub}}$ of all the sub-regions, then we conclude that the sub-region likely contains an object and this sub-region is masked. This step is critical to ensuring we are only utilizing sub-regions where a true sky-SB signal might exist. Figure 2 shows examples of how this algorithm masks sub-regions.

The final sky-SB level of a chip, S_{chip} , is the 5th-percentile of the remaining S_{sub} values. The final sky-SB rms of a chip, σ_{chip} , is the mean of all the σ_{sub} values. As shown in [SKYSURF-1](#) and [Appendix B](#) here, the 5th-percentile method on `f1t/f1c` images optimizes the rejection of sources of signal that contaminate the sky-SB signal, such as the outer parts of (large) galaxies, sky gradients (e.g. due to proximity to the Earth limb), and optical ghosts, and tends to approach the true sky-SB value from below.

3.2. ProFound Median Method

Comparing Percentile-clip and ProFound Median Methods

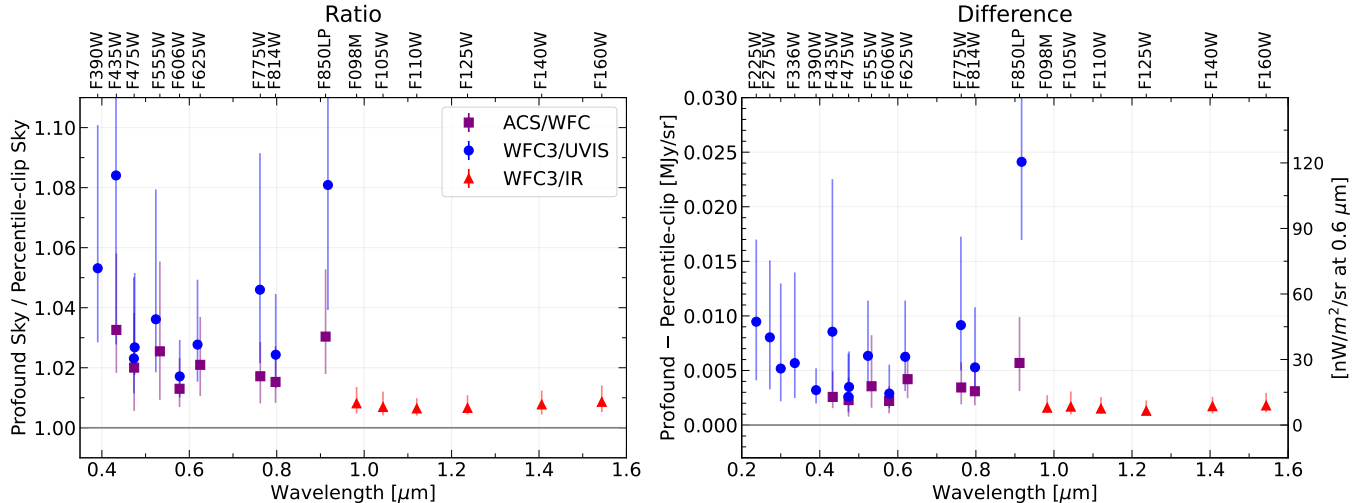


Figure 3. Comparison of the Per-clip method and the Pro-med method. The error bars show the 16th- and 84th-percentiles of the y-axis distributions. **Left:** Median ratio of the Pro-med sky-SB divided by the Per-clip sky-SB. The bluest filters are excluded because the sky-SB is nearly zero. **Right:** Median difference in Pro-Med and Per-clip method. The left y-axis shows units of MJy sr⁻¹ and the right axis shows nW m⁻² sr⁻¹ at 0.6 μ m.

The Pro-med method is similar to the Per-clip method with two main differences: 1) it calculates sky-SB values using ProFound (Robotham et al. 2018) SKY maps, and 2) it assumes the true sky to be the median of reliable sub-regions. ProFound is unique in its ability to dilate objects, remove objects, and interpolate behind them to create a robust sky map. It is able to estimate the sky-SB by using a discrete boxcar filter on a grid, then the coarse grid is bicubic interpolated to construct a sky-SB (SKY) map.

We create ProFound SKY maps for all images in the SKYSURF database. To create these SKY maps, we pass a pre-generated image mask as a dilated DQ array extension, where every flagged pixel and its immediate neighboring pixels are masked for SKY map estimation and production, along with any objects detected in the image. We run ProFound with a large box size of 1/3rd of the image dimensions, which decreases the resolution of the background maps and helps smooth over any local effects from bright objects that can leave behind features in the sky map. ProFound was run using default parameters otherwise.

The Pro-med method splits the ProFound SKY Map into sub-regions: 39×39 pixel sub-regions for WFC3/IR and 64×64 pixel sub-regions for WFC3/UVIS and ACS/WFC. Next, we calculate S_{sub} using the same method described in Section 3.1. To calculate σ_{sub} , we use the same method used to calculate S_{sub} but instead perform it using the ProFound SKY RMS map. Sub-regions are masked if the S_{sub} value for a sub-region

is greater than the minimum $S_{\text{sub}} + \sigma_{\text{sub}}$ of all the sub-regions. The final sky-SB level of a chip, S_{chip} , is the median of the unmasked S_{sub} values. We do not mask pixels flagged in the DQ mask, although we note that DQ flagged pixels are dilated and excluded from the ProFound SKY map creation. Because it uses a median, the Pro-med method tends to approach the true sky-SB value from above.

3.3. Comparison of the two methods

As shown in Figure 3, the Pro-med method gives sky-SB values that are on average 2% higher for ACS/WFC, 3% higher for WFC3/UVIS, and 0.8% higher for WFC3/IR than the Per-clip method. The difference in methods is due to the fact that the Per-clip method assumes the true sky-SB to be the darkest part of the sky (5th-percentile) while the Pro-med method assumes it to be the median. To verify this, we modify the Pro-med algorithm to use the 5th-percentile of sub-regions rather than the median, and find the median difference between methods in this test case to be $< 0.5\%$ for all ACS/WFC filters. Thus the differences seen in Figure 3 must be due to the assumptions on the nature of the true sky. The trend seen as a function of wavelength in Figure 3 is due to trends of the average sky-SB rms (Appendix H) for each filter, where a lower average sky-SB rms results in a smaller difference between methods.

We emphasize that both methods are robust and reliable depending on the science goal. SKYSURF-1 and Appendix B here show that both methods can recover the input sky-SB to within 0.4% uncertainty. The Per-clip

Uncertainty	WFC3/UVIS	WFC3/IR	ACS/WFC
Method	0.4%	0.4%	0.4%
Bias	$0.2 e^-$ (1.3%)	$0.005 e^-/s$ (1%)	$0.6 e^-$ (1.7%)
Dark	$0.3 e^-$ (2%)	$0.005 e^-/s$ (1%)	$0.5 e^-$ (1.4%)
Thermal Dark	N/A	$0.01 e^-/s$ (2.7%)	N/A
Flat-field	1%	2%	2.2%
Zeropoint	0.2%	1.5%	1%
Post-flash	$0.16 e^-$ (1%)	N/A	$0.37 e^-$ (1%)
Other	1%	0.5%	N/A
Total	3.0%	4.0%	3.4%

Table 1. SKYSURF sky-SB uncertainties. Values are listed as a percent of the sky-SB for WFC3/UVIS, WFC3/IR, and ACS/WFC. Additive errors (bias, dark, thermal dark, and post-flash) list the error in units of electrons or electrons per second, with the percent of the sky-SB for a F606W (WFC3/UVIS and ACS/WFC) or F125W (WFC3/IR) 500 second exposure shown in parenthesis. Method refers to the ability of our algorithm to retrieve the true input sky from simulated images. Bias and Dark refer to subtraction uncertainties in bias and dark frames. Thermal Dark refers to uncertainties in the Thermal Dark signal described in Carleton et al. (2022). Flat-field refers to uncertainties in flat-field correction. Zeropoint refers to uncertainties in detector zeropoints. Post-flash refers to uncertainties in post-flash subtraction. Other refers to chip differences for WFC3/UVIS and the Non-linearity of WFC3/IR.

method provides the darkest possible sky-SB for every HST image. This method is useful for subtracting the sky-SB from images where large objects take up a majority of the field of view, or where the extended profiles of discrete objects is of concern. For SKYSURF purposes, the Per-clip method measures a *lower* limit to EBL and Diffuse Light signals.

Although ProFound masks light from objects and their surroundings, excess light from large objects remains in SKYSURF ProFound SKY maps. We consider the Pro-med method to be less reliable for images where a larger portion of the field of view is contaminated by bright discrete objects. Based on tests on the simulated images and shown in Figure 12, the Pro-med method is generally a better estimator of the sky-SB for flat, empty fields where the Per-clip method is negatively biased. For SKYSURF purposes, the Pro-med method thus provides an *upper* limit to EBL and Diffuse Light signals.

We release sky-SB measurements for both methods, but the figures in this report focus on the Per-clip method as a more conservative constraint.

4. SOURCES OF UNCERTAINTY

There are many sources of uncertainty that are inconsequential for studies of discrete objects, but remain important when measuring the sky-SB. SKYSURF-1 summarizes the main SKYSURF sources of error in detail. Most uncertainties arise from subtraction of dark frames, subtraction of bias frames, and flat field corrections. We summarize these below, with some additional uncertainties discovered during the analysis of this paper. In some cases, we conduct an independent study to determine the reliability of our error estimates. Table 2 of SKYSURF-1 shows that the median exposure time in

the SKYSURF database is typically 400–600 seconds, so we utilize exposure times of 500 seconds in uncertainty analysis when needed.

Both the Per-clip and Pro-med methods are able to retrieve the input sky-SB from simulated images to within 1%. Figure 12 (Appendix B) shows that for realistic sky rms and sky gradient levels, the input sky is recoverable to within 0.4%. Following SKYSURF-1, we adopt an uncertainty in our algorithms of 0.4%.

Appendix C addresses how image anomalies, specifically crosstalk, might affect the sky-SB. We determine our algorithm is robust enough that crosstalk does not significantly affect the sky-SB. This same reasoning can be applied to other positive image anomalies, such as optical ghosts or dragon’s breath.

4.1. WFC3/UVIS Uncertainties

A bias offset is added to HST detectors to avoid presenting a negative voltage to the analog-to-digital converter. This offset is always subtracted during post-processing, and uncertainty in the bias level introduces error to the sky-SB. Figure 5 of McKay & Baggett (2017) shows a scatter in individual bias levels of ~ 0.2 electrons. For the average F606W Zodiacal sky-SB level of 22.86 AB-mag arcsec² (Table 2 of Windhorst et al. 2011) and the 0.0395 arcsec² pixel scale of the WFC3/UVIS detector, 0.2 electrons corresponds to 1.3% of Zodiacal emission for F606W for an exposure time of 500 seconds.

Since the two WFC3/UVIS detectors were carved from different wafers (unlike ACS/WFC), there is a possibility that additional uncertainties in sky-SB might appear due to inherent differences in each chip. In Appendix F, we explore differences in sky-SB levels between both

WFC3/UVIS detectors. We find that the median difference between both chips is $\sim 1\%$ in all filters.

Figure 17 from [Bourque & Baggett \(2016\)](#) shows that the scatter in determining the dark current is ~ 2 e-/hr or ~ 0.0006 e-/s. For the average F606W Zodiacal sky-SB level described above, ~ 0.0006 e-/s corresponds to a dark-current induced error in the Zodiacal sky-SB of 2% (0.3 electrons) in F606W for an exposure time of 500 seconds.

Flat-field errors are $\leq 1\%$ ([Mack et al. 2016](#)). However, errors can be larger in the corner of the UVIS1 chip where the point-spread function focus is highly variable due to the telescope breathing effects ([Sabbi & Bellini 2013](#)), and this impacts the flat field correction. Also, small offsets between the two different WFC3/UVIS detectors are present in some filters, with a maximum difference between one corner of a detector to the other of $\sim 3\%$ ([Mack et al. 2016](#)) for a few ultraviolet filters. These variations in flat-field could potentially bias our results. In Appendix E, we independently explore maximum possible uncertainties in the flat-fields by taking advantage of the large SKYSURF database. We do this by comparing the systematically darkest and brightest sub-regions, with a typical offset of 2–4%, which agrees with [Mack et al. \(2016\)](#). This is a maximum difference between the darkest and brightest sub-regions, but our algorithms automatically ignore the very darkest and brightest sub-regions. We therefore adopt the [Mack et al. \(2016\)](#) flat-field uncertainty of 1%.

We use the new photometric zeropoint calibrations explained in [Calamida et al. \(2022\)](#), where they account for variations in WFC3/UVIS zeropoints over time. We adopt the photometric errors listed in Table 8 of [Calamida et al. \(2022\)](#), which on average represent a $< 0.2\%$ 1σ dispersion (Table 8 of [Calamida et al. 2022](#)).

Charge Transfer Efficiency (CTE) trails are caused by hot pixels and charge traps that degrade the efficiency with which charge is transferred along a pixel column during the readout of the CCD. This creates a trail above the observed objects, where this effect is larger for sources further away from the readout amplifier. Different versions of the standard WFC3 calibration pipeline correct for CTE trails differently. We quantify the effects of different pipeline versions in Appendix I. We find the measured sky-SB between different versions of the pipeline to be $\sim 0.007\%$ for wavelengths longer than 0.4 microns. We therefore do not include CTE effects in our error budget.

As discussed in [SKYSURF-1](#), we adopt a post-flash subtraction error of 1%, corresponding to 0.16 electrons for a F606W image with an exposure time of 500 seconds.

To summarize WFC3/UVIS uncertainties, we consider several multiplicative and additive errors, which are itemized in Table 1. The additive uncertainties include bias subtraction (0.2 electrons), dark subtraction (0.3 electrons), and post-flash subtraction (0.16 electrons). The multiplicative uncertainties include the ability of our algorithm to estimate the sky-SB (0.4% of the sky-SB), flat-field correction (1%), zeropoint uncertainty (0.2%), and detector differences (1%).

4.2. WFC3/IR Uncertainties

During manual inspection of images, we noticed clear amplifier offsets. These effects are known to be due to differences in the noise and gain between amplifiers. In Appendix D, we explore the effect this has on sky-SB estimates. We find median differences in pixel column values close to the amplifier boundaries to be $< 0.2\%$ for all WFC3/IR filters. We therefore do not include amplifier differences in our WFC3/IR error budget.

As described in [SKYSURF-1](#), we adopt a dark/ bias uncertainty of 1% for WFC3/IR, corresponding to 0.005 electrons per second for a F125W image.

We define the thermal dark signal to be thermal noise from the telescope assembly and instruments (see [SKYSURF-2](#)). It is strongly dependent on wavelength, where it is negligible below $1 \mu\text{m}$ and significant above $1.4 \mu\text{m}$. As shown in [SKYSURF-2](#), the maximum error we expect is 2.7% for F160W, with lower uncertainties for F125W and F140W. To be conservative, we adopt a 2.7% (0.02 electrons per second) uncertainty in the thermal dark signal for all WFC3/IR sky-SB measurements in this report. Carleton et al. (in prep) will provide better constraints on the thermal dark signal.

[Mack et al. \(2021\)](#) present residuals in the sky flats of 0.5–2%. We adopt a conservative WFC3/IR flat field uncertainty of 2%.

As described in [SKYSURF-1](#), WFC3/IR photometric zeropoints have roughly remained constant to within 1.5% (rms) since 2009. Therefore, we adopt a zeropoint uncertainty of 1.5% for WFC3/IR.

As described in [The WFC3 Instrument Handbook](#), the WFC3/IR detector responds non-linearly to incident photons. The WFC3 calibration pipeline corrects for this with a $\sim 0.5\%$ uncertainty. We therefore adopt a $\sim 0.5\%$ uncertainty in the non-linearity of WFC3/IR.

WFC3/IR detector artifacts, most notably the IR blobs, are ignored by masking corresponding pixels flagged in the DQ array.

To summarize WFC3/IR uncertainties, we consider several multiplicative and additive errors, which are itemized in Table 1. The additive uncertainties include bias subtraction (0.005 electrons per second), dark subtraction

Camera	Filter	Percentile-clip Method		ProFound Median Method	
		Reliable Images [#]	Reliable Images [%]	# Reliable Images	Reliable Images [%]
ACS/WFC	F435W	8693	80	8895	81
ACS/WFC	F475W	8688	80	8855	81
ACS/WFC	F555W	2827	61	2736	59
ACS/WFC	F606W	25650	80	27423	86
ACS/WFC	F625W	2501	84	2574	87
ACS/WFC	F775W	15327	88	15697	90
ACS/WFC	F814W	44927	81	46748	84
ACS/WFC	F850LP	16309	94	16254	94
WFC3/UVIS	F225W	2014	97	2171	96
WFC3/UVIS	F275W	6712	96	7665	96
WFC3/UVIS	F300X	170	77	234	82
WFC3/UVIS	F336W	6697	91	7159	89
WFC3/UVIS	F390W	1464	85	1625	89
WFC3/UVIS	F438W	1324	78	1481	73
WFC3/UVIS	F475X	346	78	496	80
WFC3/UVIS	F475W	1543	90	1609	88
WFC3/UVIS	F555W	919	38	987	36
WFC3/UVIS	F606W	5656	77	9630	87
WFC3/UVIS	F625W	634	79	713	83
WFC3/UVIS	F775W	237	47	303	54
WFC3/UVIS	F850LP	349	96	365	95
WFC3/UVIS	F814W	7194	70	9726	75
WFC3/IR	F098M	872	79	882	81
WFC3/IR	F105W	4241	88	4227	89
WFC3/IR	F110W	3384	52	3402	53
WFC3/IR	F125W	4746	85	4763	86
WFC3/IR	F140W	4098	87	4031	88
WFC3/IR	F160W	11929	61	12352	64

Table 2. Fraction of images with reliable sky-SB measurements for every SKYSURF filter. These images are chosen using the methods of Section 5. Reliable images have no more than 30% of sub-regions flagged, contain expected noise levels based on Gaussian and Poisson noise, are not manually flagged, and are not significantly affected by persistence. We list the number of reliable sky-SB measurements and the percent of total images in the SKYSURF database that are reliable. We list these quantities for both the Per-clip Method and the Pro-med Method, which are generally in close agreement.

(0.005 electrons per second), and thermal dark corrections (0.02 electrons per second). The multiplicative uncertainties include the ability of our algorithm to estimate the sky-SB (0.4% of the sky-SB), flat-field correction (2%), zeropoint uncertainty (1.5%), and the non-linearity of the detector (0.5%).

4.3. ACS/WFC Uncertainties

ACS/WFC exhibits bias offsets that vary from amplifier to amplifier, as described in Lucas (2021). If the offsets were constant, the standard ACS/WFC calibration pipeline could remove these differences. However, the accuracy of the bias level subtraction is limited by random variations of about 0.3 DN (0.6 electrons), which corresponds to 1.7% of Zodiacal emission at F606W for

an exposure time of 500s. We therefore adopt a bias uncertainty of 1.7%.

As described in SKYSURF-1, the ACS/WFC exhibits dark current uncertainty of 0.001 e-/pix/sec. Figure 3 from Anand et al. (2022) shows a scatter in the ability to determine the ACS/WFC dark current to be ~ 0.001 electrons per second (0.5 electrons for a 500 second exposure), or 1.4% of Zodiacal emission in F606W.

Cohen et al. (2020) find that the newest ACS/WFC flat-fields result in a photometric scatter of point sources that range from 0.5% to 3%. They claim this could be contributions from various reference files and CTE losses that are underestimated. In Appendix E, and mentioned in Section 4.1, we independently explore uncertainties in the flat-fields by taking advantage of the large SKYSURF

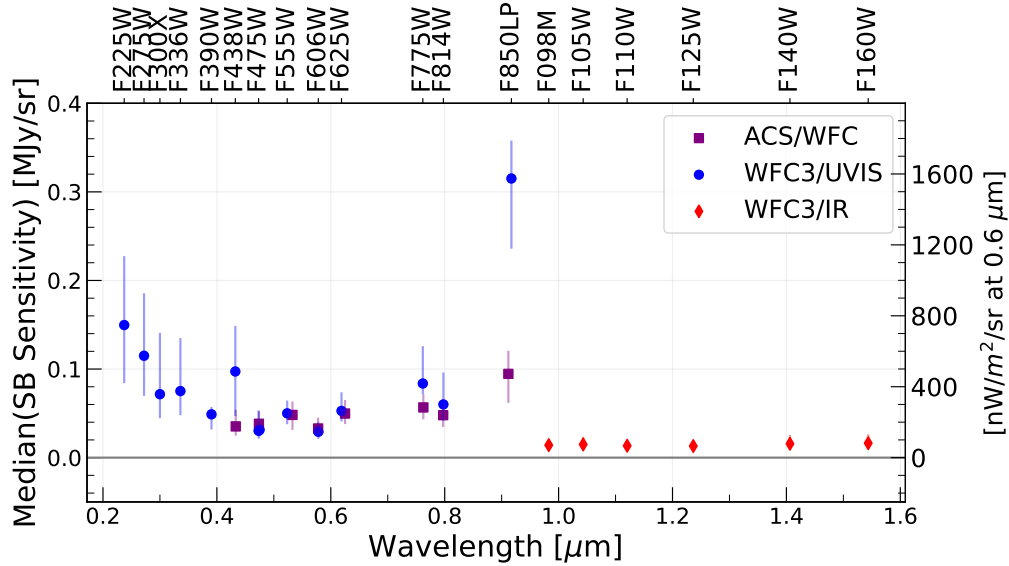


Figure 4. The median SB sensitivity for the Per-clip Method. We define the SB sensitivity to be $\text{Minimum}(\text{Sky} + \text{Sky rms}) - \text{Sky-SB}$, or the minimum $(\text{Sky} + \text{Sky rms})$ value of all the sub-regions in an image minus the measured sky-SB. Therefore, the SB sensitivity shows the cutoff where a sub-region is considered part of the background sky. The error bars show the 16th- and 84th-percentiles of the sensitivity distributions. The average SB sensitivity is $0.050 \text{ MJy sr}^{-1}$ ($23.7 \text{ AB-mag arcsec}^{-2}$) for ACS/WFC, $0.086 \text{ MJy sr}^{-1}$ ($23.1 \text{ AB-mag arcsec}^{-2}$) for WFC3/UVIS, and $0.015 \text{ MJy sr}^{-1}$ ($25.1 \text{ AB-mag arcsec}^{-2}$) for WFC3/IR.

database. On average, our results agree with Cohen et al. (2020). Following Windhorst et al. (2022), we adopt the conservative uncertainty in the ACS/WFC flat field to be 2.2%.

As described in SKYSURF-1, we adopt a zeropoint uncertainty for ACS/WFC to be 1% (Figure 2 Bohlin et al. 2020).

Current CTE corrections¹ are able to robustly subtract CTE trails for brighter objects. For fainter stars and fainter backgrounds, the CTE trail remains a positive offset. By iteratively clipping pixels, our algorithms can ignore CTE trails.

As described in SKYSURF-1, we adopt a postflash uncertainty for ACS/WFC to be 1%, or 0.37 electrons for a 500 second F606W exposure.

To summarize ACS/WFC uncertainties, we consider several multiplicative and additive errors, which are itemized in Table 1. The additive uncertainties include bias subtraction (0.6 electrons), dark subtraction (0.5 electrons), and post-flash subtraction (0.37 electrons). The multiplicative uncertainties include the ability of our algorithm to estimate the sky-SB (0.4% of the sky-SB), flat-field correction (2.2%), and zeropoint uncertainty (1%).

¹ <https://www.stsci.edu/hst/instrumentation/acs/performance/pixel-based-cte-corrections>

5. FLAGGING UNRELIABLE SKY-SB MEASUREMENTS

After performing sky-SB measurements, we filter out images where the sky-SB level is deemed unreliable, which includes measurements where the image is dominated by bright objects, images with very high sky-SB rms levels, or images where a guide star was lost. These measurements are still available for public use, but are not used in SKYSURF analysis. In this section, we describe how and why we filter unreliable sky-SB measurements. Table 2 shows the percent of images in each SKYSURF filter that are not flagged by the methods described here and are thus deemed reliable. The number of reliable images per filter is typically between 70–95%, but some filters exhibit lower reliability due to being used frequently in problematic observations (e.g. F555W is often used for stellar populations studies, and thus includes many observations of star clusters).

It is likely that a true sky-SB cannot be extracted from images that are highly saturated with bright sources, including star clusters, galaxies that take up a large portion of the field-of-view (e.g., Large Magellanic Cloud), or steep sky gradients. Since our algorithms record the number of sub-regions that are flagged as unreliable, a high number of unreliable sub-regions indicates that the sky-SB must also be unreliable. We reject sky-SB measurements where more than 30% of sub-regions are flagged as unreliable. These regions are shown as red/

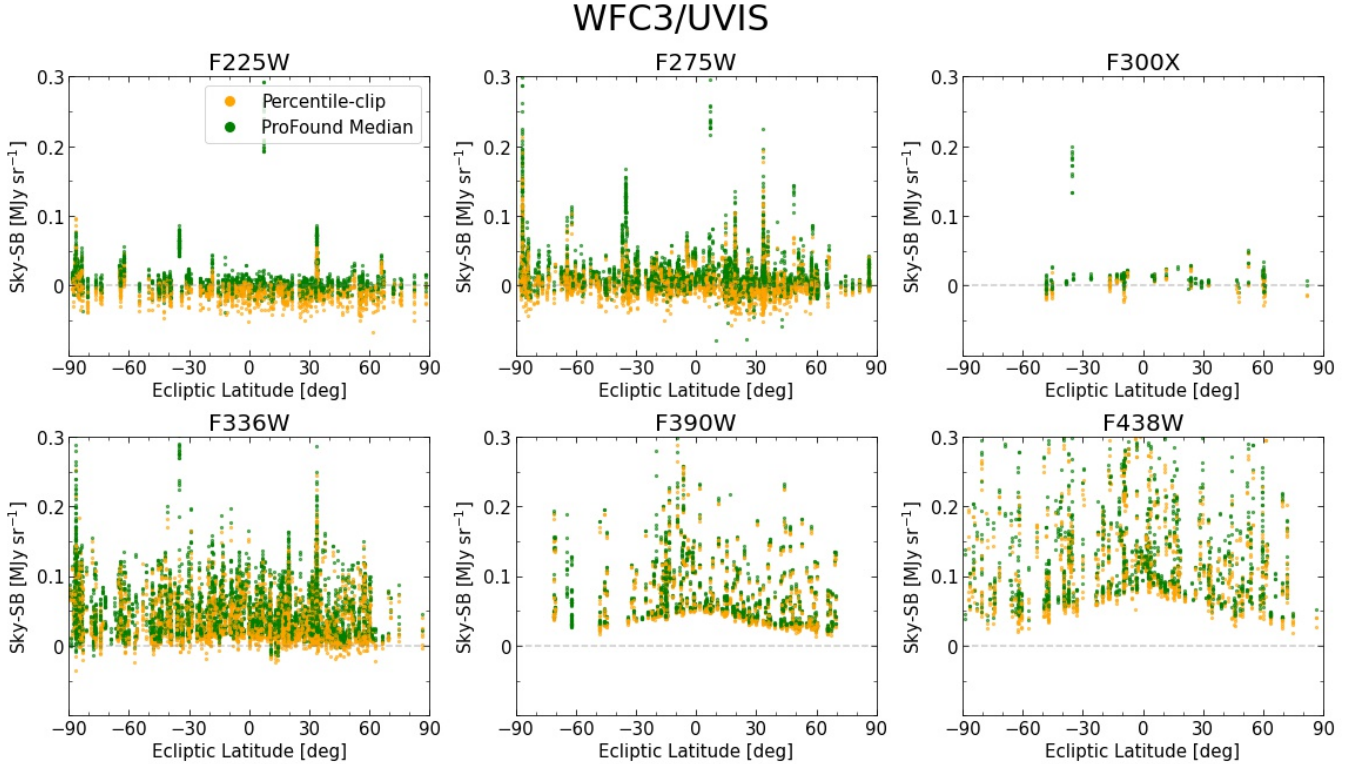


Figure 5. SKYSURF sky-SB measurements versus Ecliptic Latitude for WFC3/UVIS (UV filters), zoomed in to show the range between -0.1 to 0.3 MJy sr^{-1} .

purple in Figure 2. This condition causes differences in reliability between the Per-clip and Pro-med methods shown in Table 2. ProFound SKY maps have sources already removed. Therefore, the Pro-med algorithm will always contain different flagged sub-regions than the Per-clip method because the Per-clip method must flag sub-regions with sources.

A high sky-SB rms (σ_{chip}) can also indicate an unreliable measurement. We predict the sky-SB rms of an image to be a combination of expected Gaussian and Poisson noise:

$$\sigma_{\text{predicted}} = \frac{\sqrt{R^2 + S_{\text{chip}} \times t}}{t}, \quad (1)$$

where $\sigma_{\text{predicted}}$ is the predicted sky-SB rms in electrons per second, R is the detector readnoise in electrons, S_{chip} is the sky-SB in electrons per second, and t is the exposure time in seconds. We reject images where $\sigma_{\text{chip}} > 2\sigma_{\text{predicted}}$.

There remain cases (although rare) where the methods described above miss images that still do not have a reliable sky-SB measurement. We opted to manually inspect most of our SKYSURF images to understand how well our algorithm performs and try and identify images that are not automatically flagged. We use inspection plots like Figure 2 to manually vet our database. For

most filters, we also flagged images with satellite trails and artifacts like optical ghosts. We reject images if they are smeared (due to loss of a guide star, as identified from manual inspection), but not if they contain a satellite trail. Instead, the list of satellite trails are recorded for consideration for star and galaxy counts.

In IR detectors, an afterglow remains in pixels that were saturated in previous exposures. Referred to as persistence, this phenomenon is known to affect WFC3/IR images. Therefore, we need to ensure it does not influence our sky-SB measurements. The standard pipeline for IR images does not eliminate flux from persistence. However, the WFC3 team has developed a software that estimates the amount of persistence per `flt` file. This produces pixel maps (labeled as `_persist.fits`) estimating the amount of internal and external persistence for a given image (see Gennaro 2018). We masked pixels in 30 random F160W images with values greater than 0.005 e/s in the `_persist.fits` file and reran our sky-SB algorithm. For most images, we did not find significant differences in the sky-SB level when masking pixels affected by persistence. We found $\sim 0.25\%$ differences in sky-SB for images where more than 1% of the pixels are affected by persistence, where an affected pixel is defined to be one with $\text{Flux}_{\text{persistence}} > 0.01$ electrons per second.

WFC3/UVIS

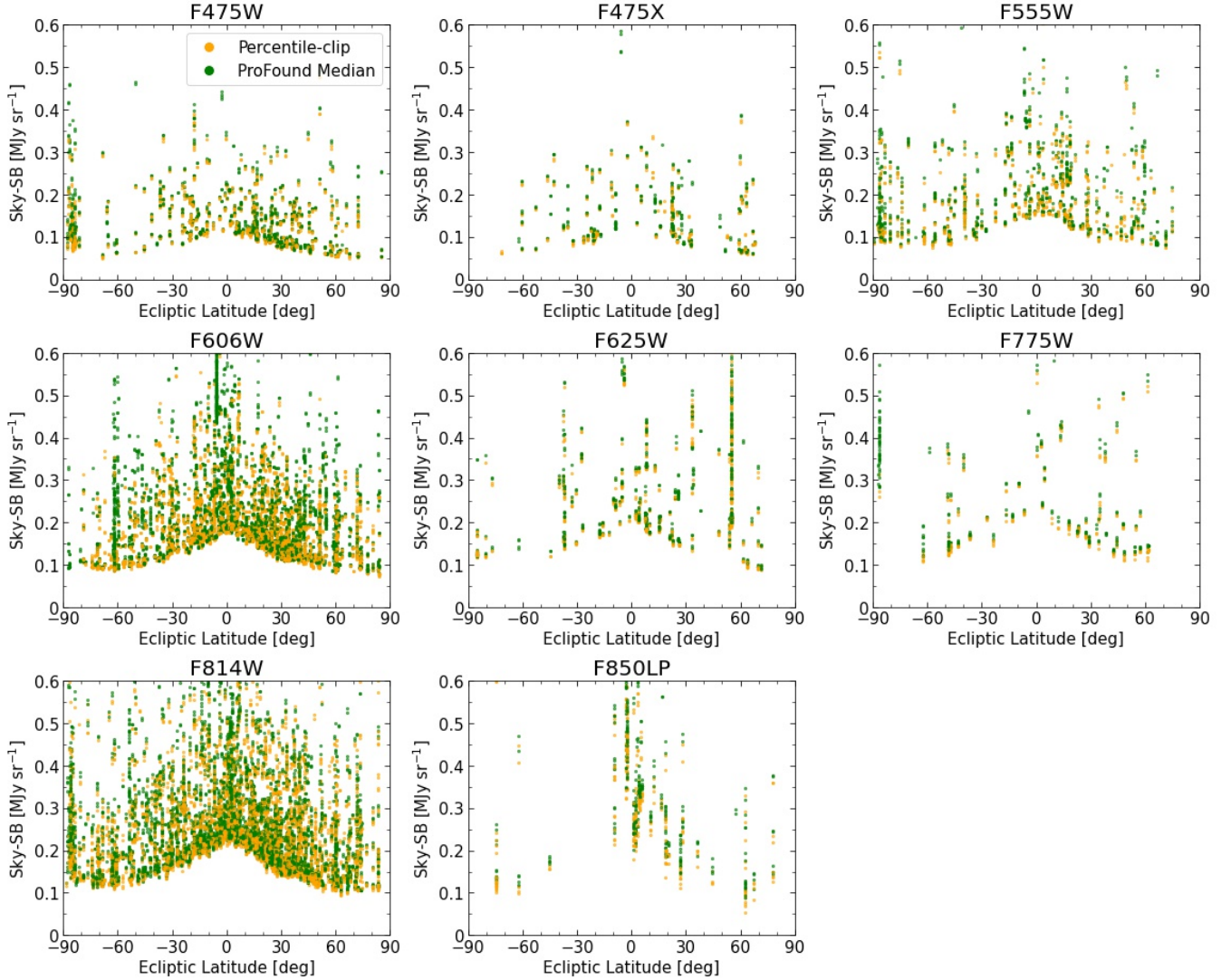


Figure 6. SKYSURF sky-SB measurements versus Ecliptic Latitude for WFC3/UVIS (Optical filters), zoomed in to show the range between 0 to 0.6 MJy sr^{-1} .

We therefore reject images where more than 1% of the pixels are affected by persistence.

6. SKY-SB MEASUREMENT RESULTS

We perform sky-SB measurements using the Per-clip and Pro-med methods, and show our results here. For all plots, we subtract from WFC3/IR estimates for the thermal dark signal as described in SKYSURF-2. These values are listed in Table 3. The process for converting our images to units of flux density is described in Appendix G.

6.1. Sky-SB Completeness

In this section, we analyze the completeness of our sky-SB measurements. We determine on average, for each

Filter	Thermal Dark	
	[e/s]	[MJy sr^{-1}]
F098M	0.0044	0.0023
F105W	0.0044	0.0013
F125W	0.0040	0.0012
F140W	0.0201	0.0050
F160W	0.0772	0.0308

Table 3. Thermal Dark values (Carleton et al., in prep) that are subtracted from sky-SB measurements in this work.

filter, how dim an extended source (i.e. a source larger than a sub-region described in Section 3) must be to be considered part of the background. We estimate our sky-SB sensitivity by finding the minimum (sky-SB + sky-SB

ACS/WFC

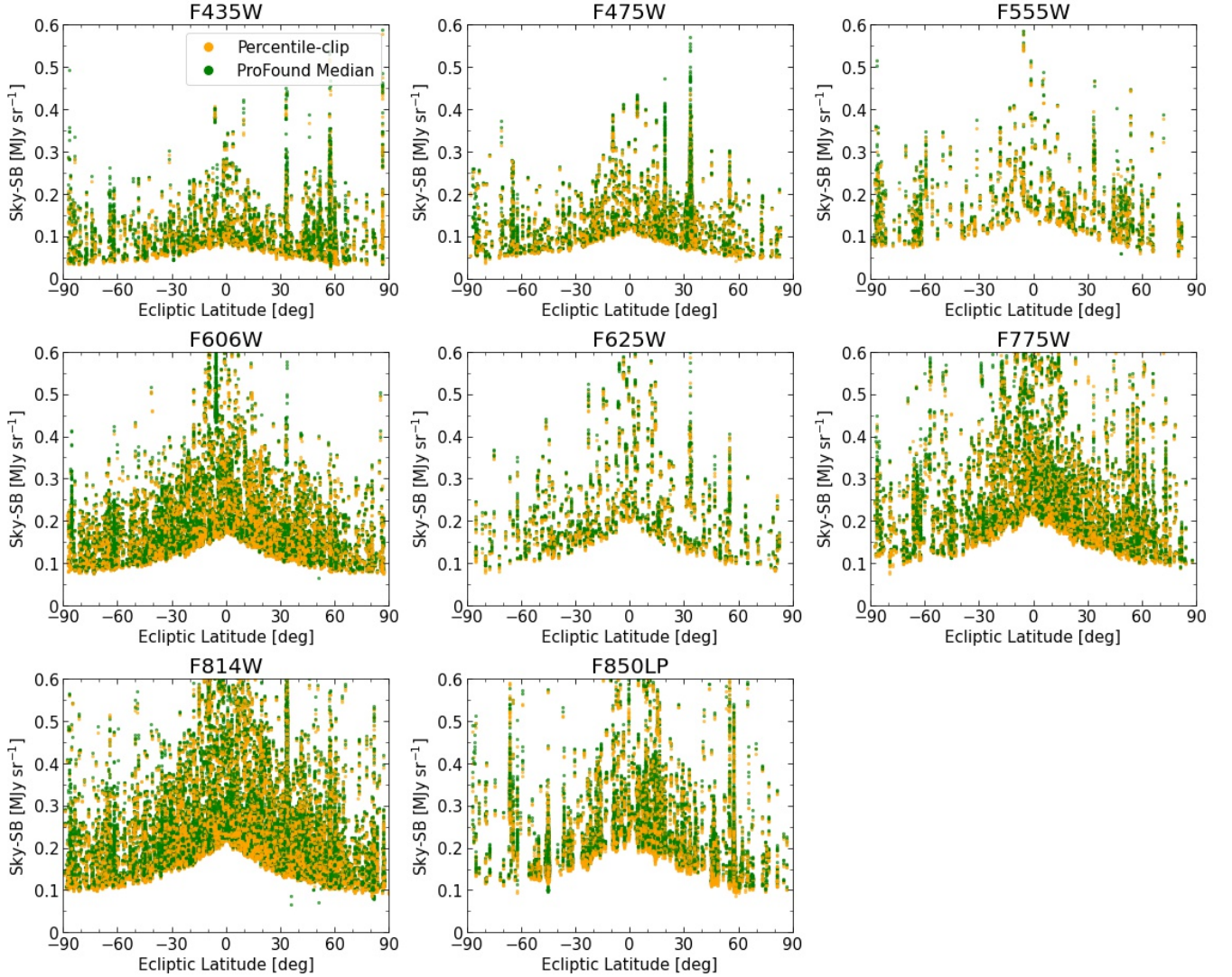


Figure 7. SKYSURF sky-SB measurements versus Ecliptic Latitude for ACS/WFC, zoomed in to show the range between 0 to 0.6 MJy sr^{-1} .

rms) of all sub-regions for an image, then subtract the sky-SB from this minimum value. This directly relates to how our algorithm flags sub-regions as containing an object.

Figure 4 shows the median sky-SB sensitivity as a function of wavelength for the Per-clip method. As with Figure 3, the trends seen as a function of wavelength is due to trends in the average sky-SB rms for each filter (Appendix H), where a lower average sky-SB rms results in a lower sensitivity. For a particular wavelength, a sub-region (or extended object) with a sky-SB that is brighter than the sensitivities shown in Figure 4 will be identified as an object. If a sub-region has a sky-SB that is fainter than the sensitivities shown in Figure 4, it will be considered part of the background.

Since extended discrete objects are often measured in $\text{AB-mag arcsec}^{-2}$, we include the average sky-SB sensitivity threshold in these units here and in the caption of Figure 4. The average SB sensitivity is $0.050 \text{ MJy sr}^{-1}$ ($23.7 \text{ AB-mag arcsec}^{-2}$) for ACS/WFC, $0.086 \text{ MJy sr}^{-1}$ ($23.1 \text{ AB-mag arcsec}^{-2}$) for WFC3/UVIS, and $0.015 \text{ MJy sr}^{-1}$ ($25.1 \text{ AB-mag arcsec}^{-2}$). The average WFC3 sensitivity is less complete than ACS because it includes the UV filters, where the sensitivity is higher. The WFC3/UVIS F850LP point appears significantly higher than the other points due to the higher average sky-SB. For WFC3/UVIS F850LP reliable images, the average Ecliptic Latitude is ~ 5 deg (see Figure 6), where the average Ecliptic Latitude for the other WFC3/UVIS filters is ~ 30 deg. With a majority of the images being at

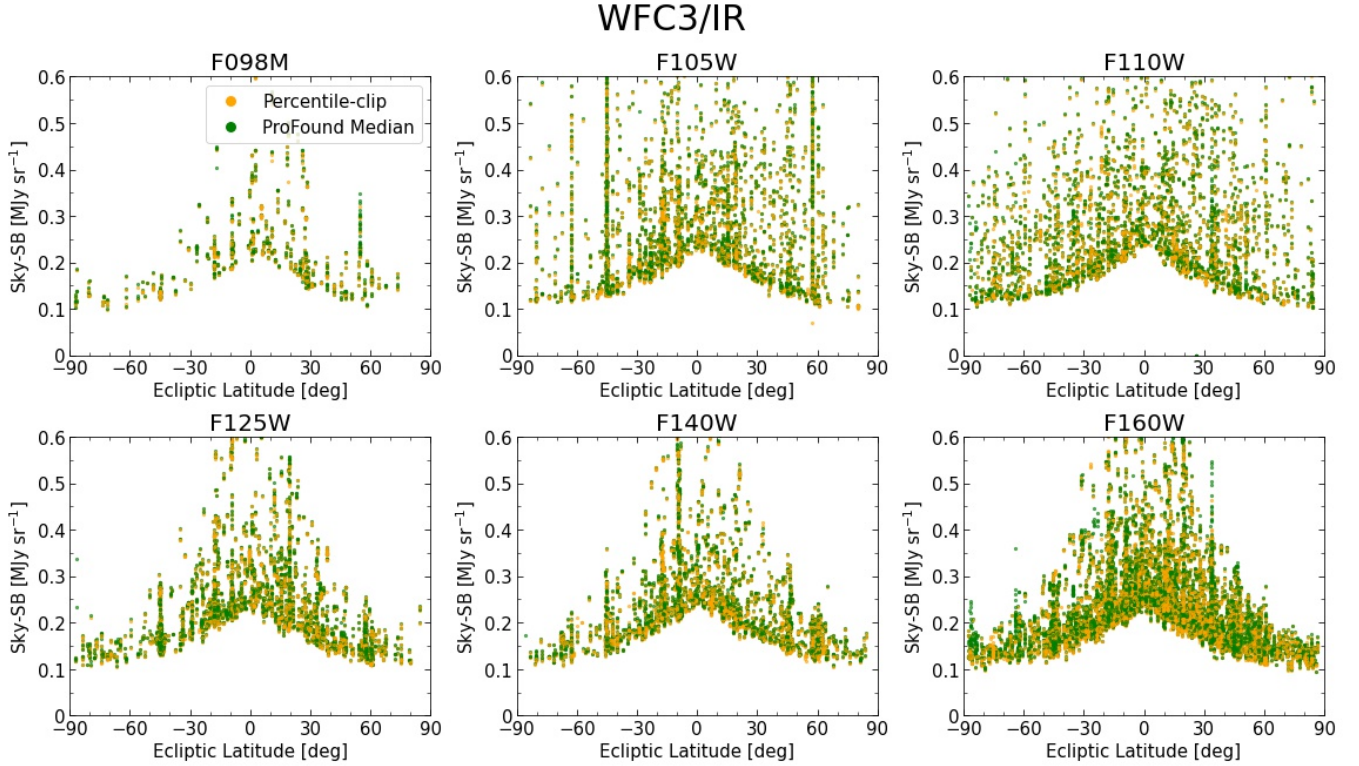


Figure 8. SKYSURF sky-SB measurements versus Ecliptic Latitude for WFC3/IR, zoomed in to show the range between 0 to 0.6 MJy sr^{-1} .

low Ecliptic latitudes where ZL emission is the brightest, the sky-SB is higher and the sky-SB sensitivity is also higher.

6.2. Sky-SB versus Ecliptic Latitude

Figures 5–8 show our results as a function of Ecliptic Latitude for both methods. The Interplanetary Dust Cloud is densest near the ecliptic plane, thus raising sky-SB values there. In all filters, there are close to zero outliers that fall below the expected trend, showcasing that we are able to successfully exclude unreliable low sky-SB measurements. There are “chimneys” present, where there will be many images at the same location with relatively high sky-SB levels. These are sometimes due to observations of galaxies and nebulae that take up a majority of the field of view, but are often due to varying Sun Angles, where lower Sun Angles can raise sky-SB levels (see Figure 10). For example, M31 (the Andromeda Galaxy) is located at an Ecliptic Latitude of $b \simeq 34^\circ$, and can therefore account for the tall chimney seen at $b \simeq 34^\circ$ in the F814W filter of Figure 7.

The Per-clip measurements fall below zero in UV wavelengths, possibly indicating that the Pro-med method is more reliable in this wavelength regime. Since the sky-SB is much darker, and there are far fewer object photons at UV wavelengths, the average exposure is

significantly less crowded with objects and the Per-clip method might underestimate the sky-SB. Additionally, the measurement noise in UV wavelengths is larger than at other wavelengths, as shown in Appendix H. This effect will also cause the Per-clip method to be biased with respect to the true value. Figure 12 shows that the Per-clip method underestimates the true sky-SB by a larger margin as the sky-SB rms increases.

6.3. Sky-SB SED

To best understand trends in sky-SB, we create a spectral energy distribution (SED) of the darkest observed sky-SB at HST wavelengths. Figure 9 shows our sky-SB SED, where each SKYSURF point is a 3σ -clipped median of all sky-SB measurements within 30° from the Ecliptic poles (the darkest sky), and excluding images within 20° from the Galactic plane. To account for brighter images due to Earthshine, images with Sun Altitudes greater than zero are also ignored, where Sun Altitude is defined as the angle of the Sun above the Earth’s horizon at the time of observation. To account for higher sky-SB levels due to low Sun Angles (see SKYSURF-1), we ignore images with Sun Angles less than 80° . The Sun Angle cut is not used for the bottom panel of Figure 10. Finally, we exclude observations where we know the sky-SB will be high due to large, extended objects. Specifically, we

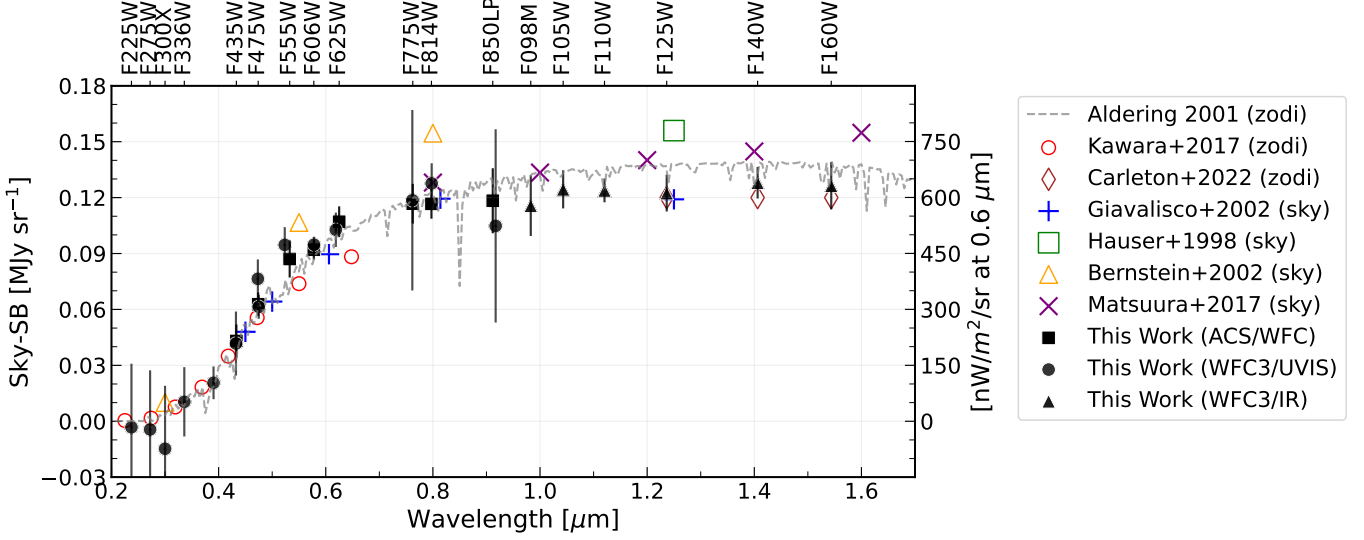


Figure 9. SKYSURF SED using Per-clip sky-SB measurements, for Ecliptic latitudes within 30 deg of the poles. Each black point is a ACS/WFC (square), WFC3/UVIS (circle) or WFC3/IR (triangle) 3σ -clipped median sky-SB measurement. We exclude images taken within 20° of the Galactic plane, images taken with Sun Altitude’s greater than 0° , images taken with Sun Angles less than 80° , and images that contain a common extended object in the target name. The error bar is the standard error in unique positions in the sky and the sky-SB measurement error, added in quadrature (see Equation 3). We compare our measurements to previous measurements of the sky-SB (Giavalisco et al. 2002; Hauser et al. 1998; Bernstein et al. 2002; Matsuura et al. 2017), a model of Zodiacal emission (Aldering 2001), and measurements of Zodiacal emission (Kawara et al. 2017; Carleton et al. 2022).

ignore images where M31, SMC, LMC, M32, M33, NGC, or N44 appear in the target name.

We take into account that there can be many observations in the same part of the sky, which could bias a sky-SB measurement for a single filter. We take the median sky-SB of all observations taken within 10 arcmin of each other, and define each of these 10 arcmin groups as a unique position. Each SKYSURF point in Figure 10 represents the 3σ -clipped median of all unique positions for every HST filter. The error bars are a combination of the standard error in sky-SB values along different unique positions (σ_{spread}), and the sky-SB error (σ_{sky}):

$$\sigma_{\text{spread}} = \frac{\text{std}}{\sqrt{\# \text{ of Unique Positions}}}, \quad (2)$$

$$\text{Error Bar} = \sqrt{\sigma_{\text{spread}}^2 + \sigma_{\text{sky, clipped}}^2}, \quad (3)$$

where “std” is the standard deviation in sky-SB values, and $\sigma_{\text{sky, clipped}}$ is a 3σ -clipped median of all sky-SB measurement errors (Table 1). If there is only one unique position for a particular filter, this filter is not plotted.

We compare our sky SED in Figure 9 to several different measurements of the dark sky-SB and estimates of ZL emission. SKYSURF measurements are shown as filled black squares (ACS/WFC), circles (WFC3/UVIS) or triangles (WFC3/IR). The grey dashed line represents the parametric ZL emission model from Aldering

(2001) (which is a modification of the Leinert et al. (1998) model). We plot this using the `gunagala` sky module (Robitaille et al. 2022). Kawara et al. (2017) measurements of ZL emission taken with the HST’s Faint Object Spectrograph are shown as open red circles. The open brown diamonds represent the brightest ZL emission estimates using the Kelsall et al. (1998) ZL model, estimated from Figure 3 of SKYSURF-2. Giavalisco et al. (2002) present sky-SB measurements scaled to the North Ecliptic Pole (NEP), shown as blue plus signs, which include measurements from Leinert et al. (1998), the HDF Team, Wright (2001), and Aldering (2001). The Hauser et al. (1998) sky-SB measurement, shown as an open green square, represents the COBE/ DIRBE sky-SB measurement that includes all EBL. The open orange triangles show dark sky HST WFPC2 measurements from Bernstein et al. (2002). This measurement excludes EBL coming from stars and galaxies with total magnitudes brighter than $AB \simeq 23$ mag (in WFPC2 F555W filter). Finally, the purple X’s represent sky spectra approximated from Figure 2 of Matsuura et al. (2017), which were measured using the Low-resolution Spectrometer on the Cosmic Infrared Background Experiment (CIBER).

Overall, Figure 9 highlights the need for Project SKYSURF, as no sky-SB measurements across the entire UV-to-Near-IR range exist. The shape of our sky-SB

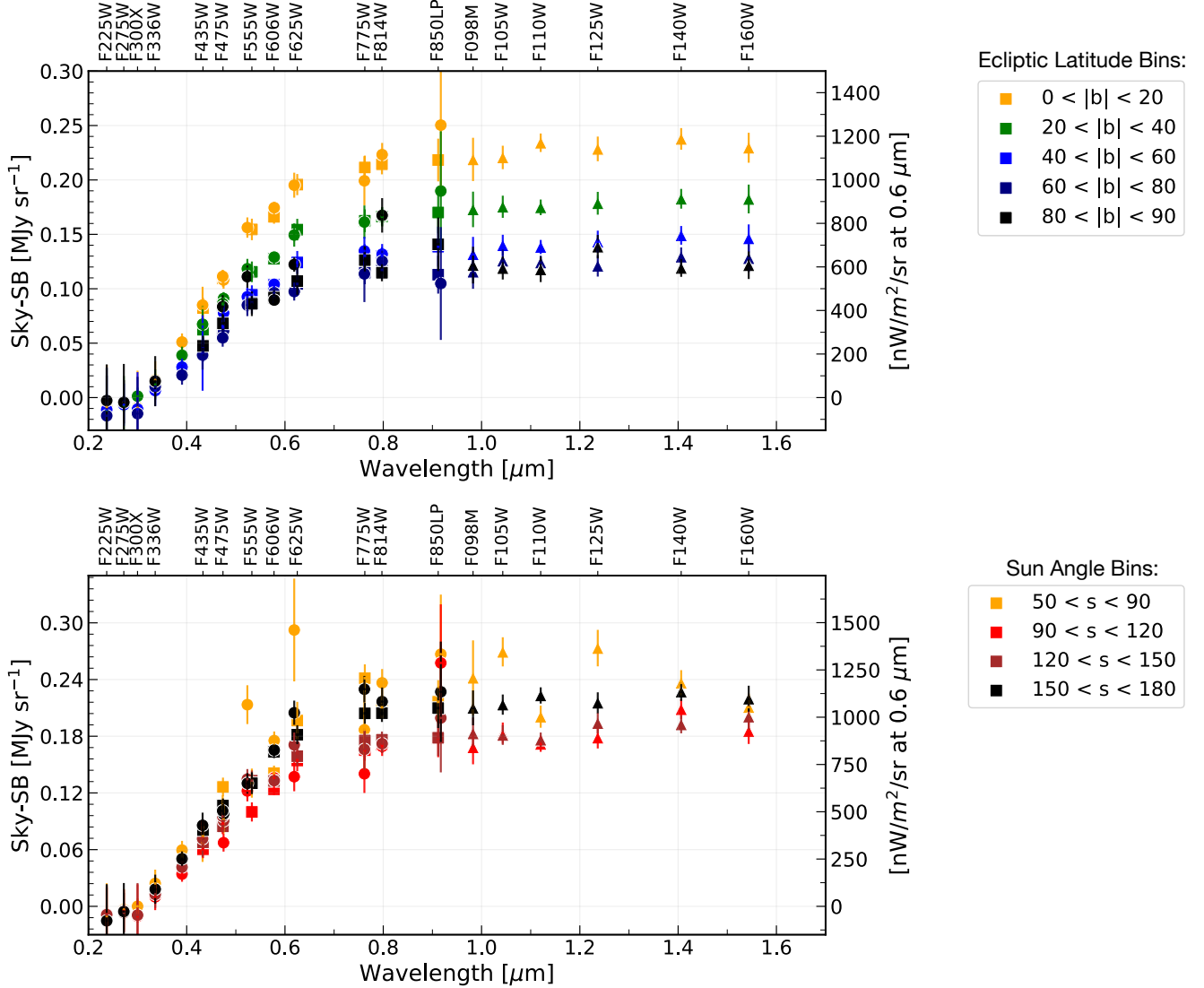


Figure 10. SKYSURF SED using Per-clip sky-SB measurements, for different Ecliptic Latitude (b , where each bin includes the absolute value of b) and Sun Angle (s) bins. Each point is a ACS/WFC (squares), WFC3/UVIS (circles) or WFC3/IR (triangles) 3σ -clipped median sky-SB measurement. We exclude images taken within 20° of the Galactic plane, images taken with Sun Altitude's greater than 0° , and images that contain a common extended object in the target name. The error bars are scaled in the same way described in Figure 9.

measurements agree well with other models and predictions, although some differences are still present.

At wavelengths shortward of $0.5 \mu\text{m}$, our sky-SB measurements agree with Kawara et al. (2017), Bernstein et al. (2002), and Giavalisco et al. (2002). This indicates that the amount of EBL present at UV wavelengths is small. The F300X filter falls below the expected range, but there are only three unique positions representing this point. As discussed in Section 3, this reiterates that the Per-clip method likely underestimates the sky-SB in UV wavelengths, especially when there are not enough unique positions represented.

Between $0.5 \mu\text{m}$ and $0.8 \mu\text{m}$, some SKYSURF measurements do not seem to agree with other measurements. The Bernstein et al. (2002) points are expected to be higher since their measurements include the flux from objects fainter than $AB \simeq 23$ mag, where SKYSURF excludes the flux from all resolved objects. The F555W and F475W filters are often used for stellar population studies, and thus contains many observations of nebulae and star clusters that can raise the sky-SB level. Both of these WFC3/UVIS filters contain images of the Large Magellanic Cloud that were not automatically filtered out by target name, thus raising the measured sky-SB. Additionally, many WFC3/UVIS measurements (e.g.,

WFC3/UVIS F775W) are less reliable because they have significantly fewer reliable images (see Table 2). The offset between SKYSURF measurements and Kawara et al. (2017) indicates a potential for some Diffuse Light signal between 0.5 μm and 0.8 μm .

SKYSURF points greater than 0.8 μm agree with other measurements, although the Aldering (2001) ZL model appears to overestimate sky-SB levels in the Near-IR. The COBE/DIRBE sky-SB measurement (Hauser et al. 1998) is brighter because it includes all EBL, while our sky-SB measurements ignores discrete objects. The CIBER (Matsuura et al. 2017) measurements also include all EBL flux. If we instead compare to the Kelsall et al. (1998) ZL model using the three SKYSURF-2 points, there still remains a possibility of a Diffuse Light signal. We estimate a new Diffuse Light signal using these measurements in Section 7.

The top panel of Figure 10 displays our sky-SB SED for different ecliptic latitude bins. We find the shape of the sky-SB SED to be similar at all ecliptic latitudes.

The bottom panel of Figure 10 displays the sky-SB SED for different Sun Angle bins. Sun Angle (sometimes also referred to as Solar Elongation) is defined as the angle between an observation and the Sun. Caddy et al. (2022) and Leinert et al. (1998) show that Sun Angle can influence the brightness of Zodiacal emission, and thus the observed sky-SB. We find the shape of our sky-SB SED to depend on Sun Angle at wavelengths between 0.9–1.4 μm . For low Sun Angles (orange points), we observe a brighter sky-SB that peaks around 1 μm , although these measurements are highly variable since a low Sun Angle is generally not preferred with HST. At higher Sun Angles, the sky-SB SED flattens between 0.9–1.4 μm . Our results agree with previous models about Zodiacal scattering, where we find the scattering of Solar photons off interplanetary dust to not be isotropic. Specifically, our results suggest that the anisotropy of the scattering phase function changes as a function of wavelength. Appendix J compares our SKYSURF sky-SB measurements to the Aldering (2001) ZL emission prediction, as a function of Sun Angle. These results agree with Figure 10.

7. UPDATED DIFFUSE LIGHT LIMITS

We compare our sky-SB measurements to those presented in SKYSURF-2 (for F125W, F140W and F160W) to estimate new preliminary Diffuse Light (DL) limits based on the Kelsall et al. (1998) Zodiacal model. The DL limits from SKYSURF-2 are estimated using the Lowest Fitted Sky (LFS) method, where they fit a *sech* curve to the darkest thermal-dark corrected sky-SB values measured for SKYSURF. They fit a similar curve

to the Kelsall et al. (1998) ZL emission predictions and estimate a DL signal by comparing the two curves. DGL and unresolved EBL still present in HST images is also subtracted during this process.

We calculate the median ratio and median difference in reliable sky-SB values between the sky-SB measurements in this work and the sky-SB measurements used in SKYSURF-2. By doing this, we can update the preliminary DL limits from SKYSURF-2. In Appendix K, we confirm that the median difference is a good representation of the darkest sky-SB measurements used in SKYSURF-2. Our DL limits are shown in Table 4.

The sky-SB measurements in this work are 1.5–3% lower than the F125W, F140W, and F160W measurements in SKYSURF-2, resulting in DL limits that are typically 50–67% lower than the conservative limits from SKYSURF-2. The Per-clip method estimates DL limits of 0.006 MJy sr⁻¹ (14 nW m⁻² sr⁻¹), 0.013 MJy sr⁻¹ (28 nW m⁻² sr⁻¹), and 0.009 MJy sr⁻¹ (17 nW m⁻² sr⁻¹) for F125W, F140W, and F160W, respectively. The Pro-med method estimates DL limits of 0.007 MJy sr⁻¹ (18 nW m⁻² sr⁻¹), 0.015 MJy sr⁻¹ (32 nW m⁻² sr⁻¹), and 0.011 MJy sr⁻¹ (21 nW m⁻² sr⁻¹) for F125W, F140W, and F160W, respectively. These methods are in excellent agreement with one another, with differences in the expected sense described in Section 3. We adopt the same error from SKYSURF-2: 0.005 MJy sr⁻¹. Overall, these estimates provide the most stringent all-sky constraints in this wavelength range, and show a significant Diffuse Light component of unknown origin.

SKYSURF’s large database gives us the unique ability to independently and consistently derive galaxy counts (and therefore create a SKYSURF EBL model), as well as constrain ZL emission at HST wavelengths. We can compare our sky-SB measurements to a SKYSURF EBL model based on galaxy counts and a SKYSURF ZL emission model for a final estimate of DL. The DL limits presented here are designed to be conservative, and measurements of DL using an updated Zodiacal model for the entire HST wavelength range will be provided in future papers.

8. PUBLIC DATA PRODUCTS

We provide several data products on the official SKYSURF website². Relevant to this paper are: 1) Sky-SB measurements for all SKYSURF images, and 2) FITS files containing the sky sub-regions used for the Per-clip method. In this section, we describe these products. In addition to the sky-SB data products described below,

² <http://skysurf.asu.edu>

Filter	F125W	F140W	F160W
SKYSURF-2 DL Limit [MJy sr⁻¹]	0.0122	0.0182	0.0148
Ratio: Per-clip Sky-SB / SKYSURF-2 Sky-SB	0.970	0.977	0.976
Difference: Per-clip Sky-SB – SKYSURF-2 Sky-SB [MJy sr ⁻¹]	-0.006	-0.005	-0.006
This Work: Per-clip DL Limit [MJy sr⁻¹]	0.006	0.013	0.009
Ratio: Pro-med Sky-SB / SKYSURF-2 Sky-SB	0.978	0.985	0.984
Difference: Pro-med Sky-SB – SKYSURF-2 Sky-SB [MJy sr ⁻¹]	-0.005	-0.003	-0.004
This Work: Pro-med DL Limit [MJy sr⁻¹]	0.007	0.015	0.011

Table 4. Updated SKYSURF Diffuse Light limits. We compare sky-SB measurements for F125W, F140W, and F160W from SKYSURF-2 to sky-SB measurements presented in this work. The second row lists the DL limits from SKYSURF-2. The third row shows the median ratio between reliable (as defined in Section 5) Per-clip sky-SB measurements and those from SKYSURF-2. The fourth row shows the difference in these sky-SB values, in units of MJy sr⁻¹. We subtract this difference from the SKYSURF II DL limit to estimate a DL limit based on the Per-clip algorithm, shown in the fifth row. Rows 3-5 are repeated for the Pro-med algorithm in Rows 6-8. We adopt the same error from SKYSURF-2: 0.005 MJy sr⁻¹.

we provide ProFound SKY maps and SKYSURF drizzled images (see SKYSURF-1).

8.1. Sky-SB Data Tables

For every image, we provide SKYSURF sky-SB measurements in the native units of the `flt/flc` files, as well as in calibrated flux units of MJy sr⁻¹. The process for converting our images to units of flux density is described in Appendix G. Estimates of the thermal dark levels will be presented in Carleton et al. (in prep) and are included in the public files for all WFC3/IR measurements. We provide sky-SB measurements with and without thermal dark corrections.

We include an uncertainty for each sky-SB measurement using Table 1. The error is calculated as following:

$$\sigma_{\text{sky}} = \sqrt{\sigma_{\text{add}}^2 + (\sigma_{\text{mult}} \times S_{\text{chip}})^2}, \quad (4)$$

where σ_{sky} is the total sky-SB error in units of electrons or electrons per second, σ_{add} is the additive error in units of electrons or electrons per second, σ_{mult} is the multiplicative error in units of percent, and S_{chip} is the measured sky-SB in units of electrons or electrons per second. This error is converted to MJy/sr using the methods described in Appendix G.

Every sky-SB measurement has a corresponding flag that designates images with too many bad sub-regions, too high of a sky-SB rms, images marked during the manual inspections, located within galactic plane, located close to the Earth’s limb, located at high Sun Altitude’s, contains a large common object, or has too many pixels affected by persistence. We refer to corresponding documentation on the public files for more information.

8.2. Subregion FITS Files

The Pro-med method requires ProFound SKY maps, and therefore these maps have been created for all images in the SKYSURF database. These will be publicly

available for users who wish to inspect the background sky models. For users who decide to utilize the Per-clip method instead, we provide FITS files containing the sub-regions created during the Per-clip algorithm. Each fits file, which we refer to as a SUB file, has a single sky value associated with each sub-region where each sub-region takes up a single pixel. So for a 1014 × 1014 pixel WFC3-IR image that is divided into 26 × 26 pixel sub-regions, the corresponding SUB image will be 26 × 26 pixels in size.

They contain one primary header and two data extensions. The primary header is copied from the original `flt/flc` image, where the extension name (EXTNAME) is changed to SUB_SKY. The two data extensions are labeled ‘SKY’ and ‘RMS’ and contain the sky and sky RMS sub-region data. In the SKY and RMS extensions only, WCS keywords are listed in pixel units corresponding to the new SUB image pixels, rather than the original `flt/flc` image pixels.

9. CONCLUSION

We present sky-SB algorithms and measurements for project SKYSURF, an HST archival program with the end goal of constraining an all-sky EBL signal. The SKYSURF database includes more than 200,000 HST images, spanning 0.2–1.7 μm. In this paper, we measure the sky-SB using HST’s three main cameras: ACS/WFC, WFC3/UVIS, and WFC3/IR. This includes over 75,000 ACS/WFC images, over 20,000 WFC3/UVIS images, and over 40,000 WFC3/IR images.

We utilize two algorithms to measure the sky-SB: the Per-clip Method and the Pro-med method (Figure 1). The Per-clip method uses `flt/flc` files, while the Pro-med method uses ProFound SKY maps. Both methods divide each HST image into many sub-regions, then exclude sub-regions that likely don’t contain a true sky-SB signal due to object contamination (Figure 2). As calibrated in Section 4.2 of SKYSURF-1 and Appendix B

here, the Per-clip Method assumes the true sky-SB to be the 5th-percentile of reliable sub-regions, while the Pro-med Method assumes the true sky-SB to be the median of reliable sub-regions. Both methods can extract the true input sky-SB from a simulated WFC3/IR F125W image to within 1%.

We find that Per-clip sky-SB measurements are typically $\sim 2-3\%$ lower than Pro-med sky-SB measurements (Figure 3). Although both methods are robust, the science goal and type of image should determine which method is more reliable.

SKYSURF sources of error are summarized in Table 1. We reject images with too many bad sub-regions, too high of a measured rms, and too much persistence. The typical percent of reliable images for each filter is 70–90% (Table 2). Images with unreliable sky-SB measurements are still released to the public, but should not be used for EBL estimates.

In Figure 4, we show the completeness of our sky-SB measurements, or the SB an extended object must be to be detected as an object via our algorithms. The average SB completeness ranges from $0.015 \text{ MJy sr}^{-1}$ to $0.086 \text{ MJy sr}^{-1}$ ($25.06 \text{ AB-mag arcsec}^{-2}$ to $23.13 \text{ AB-mag arcsec}^{-2}$).

Figures 5 – 10 show our sky-SB measurement results. As a function of ecliptic latitude, sky-SB measurements follow expected trends by peaking near the ecliptic plane. There are almost no outliers, highlighting the success of our ability to filter our unreliable sky-SB measurements. The sky-SB SED shows that our measurements agree well with some other measurements, but methods to measure the sky-SB and estimate ZL emission are still poorly understood.

As shown in Table 4, we estimate DL limits based on the methods of SKYSURF-2 for F125W, F140W, and F160W. To do this, we calculate the median difference between the sky-SB measurements in this work and those used in SKYSURF-2, and subtract this value from the DL limits presented in SKYSURF-2. The DL limits in SKYSURF-2 are conservative, and the DL limits in this work are typically 50% - 67% of those in SKYSURF-2. Across both the Per-clip method and Pro-med method, our DL limits range from $0.006 \text{ MJy sr}^{-1}$ to $0.015 \text{ MJy sr}^{-1}$.

We summarize SKYSURF data products that will be released to the public in Section 8. These include tables of all SKYSURF sky-SB measurements, as well as FITS files that show the Per-clip sub-regions.

These sky-SB measurements hopefully not only benefit Project SKYSURF, but will help the community as well. The algorithms presented here provide methods to extrapolate a reliable sky-SB level that can be subtracted from images for reliable photometry. The Per-clip method proves especially useful for low surface-brightness studies, where it is imperative that signal from real objects does not contaminate the measured sky-SB.

These results are the first step to achieving SKYSURF’s end goal of constraining an EBL signal using HST’s vast archive of data. Next steps of the project include source counts using the entire SKYSURF database, updated Thermal Dark signals, constraining a Zodiacal model utilizing SKYSURF data, and measuring an EBL signal using these results.

ACKNOWLEDGEMENTS

All of the data presented in this paper were obtained from the Mikulski Archive for Space Telescopes (MAST). This project is based on observations made with the NASA/ESA Hubble Space Telescope and obtained from the Hubble Legacy Archive, which is a collaboration between the Space Telescope Science Institute (STScI/NASA), the Space Telescope European Coordinating Facility (ST-ECF/ESA), and the Canadian Astronomy Data Centre (CADM/NRC/CSA).

We acknowledge support for HST programs AR-09955 and AR-15810 provided by NASA through grants from the Space Telescope Science Institute, which is operated by the Association of Universities for Research in Astronomy, Incorporated, under NASA contract NAS5-26555. Work by RGA was supported by NASA under award number 80GSFC21M0002.

We especially thank the entire SKYSURF team for their contributions to making this project successful.

We also acknowledge the indigenous peoples of Arizona, including the Akimel O’odham (Pima) and Pee Posh (Maricopa) Indian Communities, whose care and keeping of the land has enabled us to be at ASU’s Tempe campus in the Salt River Valley, where this work was conducted.

Software: Astropy (Astropy Collaboration et al. 2013, 2018, 2022)

Software: ProFound (Robotham et al. 2018)

Software: GalSim (Rowe et al. 2015)

REFERENCES

Aldering, G. 2001, LBNL report, LBNL-51157, 1, doi: <http://www-supernova.lbl.gov/~aldering/>

Anand, G., Grogin, N., & Anderson, J. 2022, Revisiting ACS/WFC Sky Backgrounds, Instrument Science Report ACS 2022-1

- Andrews, S. K., Driver, S. P., Davies, L. J., Lagos, C. d. P., & Robotham, A. S. G. 2017, arXiv, 474, 898–916, doi: [10.1093/mnras/stx2843](https://doi.org/10.1093/mnras/stx2843)
- Arendt, R. G., Odegard, N., Weiland, J. L., et al. 1998, arXiv, 508, 74–105, doi: [10.1086/306381](https://doi.org/10.1086/306381)
- Ashcraft, T. A., Windhorst, R. A., Jansen, R. A., et al. 2018, PASP, 130, 064102, doi: [10.1088/1538-3873/aab542](https://doi.org/10.1088/1538-3873/aab542)
- Ashcraft, T. A., McCabe, T., Redshaw, C., et al. 2022, arXiv e-prints, arXiv:2208.14572, <https://arxiv.org/abs/2208.14572>
- Astropy Collaboration, Robitaille, T. P., Tollerud, E. J., et al. 2013, A&A, 558, A33, doi: [10.1051/0004-6361/201322068](https://doi.org/10.1051/0004-6361/201322068)
- Astropy Collaboration, Price-Whelan, A. M., Sipőcz, B. M., et al. 2018, AJ, 156, 123, doi: [10.3847/1538-3881/aabc4f](https://doi.org/10.3847/1538-3881/aabc4f)
- Astropy Collaboration, Price-Whelan, A. M., Lim, P. L., et al. 2022, apj, 935, 167, doi: [10.3847/1538-4357/ac7c74](https://doi.org/10.3847/1538-4357/ac7c74)
- Bernstein, G. M., Nichol, R. C., Tyson, J. A., Ulmer, M. P., & Wittman, D. 1995, AJ, 110, 1507, doi: [10.1086/117624](https://doi.org/10.1086/117624)
- Bernstein, R. A. 2007, The Astrophysical Journal, 666, 663–673, doi: [10.1086/519824](https://doi.org/10.1086/519824)
- Bernstein, R. A., Freedman, W. L., & Madore, B. F. 2002, The Astrophysical Journal, 571, 56–84, doi: [10.1086/339422](https://doi.org/10.1086/339422)
- Bertin, E., & Arnouts, S. 1996, A&AS, 117, 393, doi: [10.1051/aas:1996164](https://doi.org/10.1051/aas:1996164)
- Bickel, D. R., & Fruehwirth, R. 2005, arXiv Mathematics e-prints, math/0505419, <https://arxiv.org/abs/math/0505419>
- Biretta, J., & Baggett, S. 2013, WFC3 Post-Flash Calibration, Space Telescope WFC Instrument Science Report
- Bohlin, R. C., Ryon, J. E., & Anderson, J. 2020, Update of the Photometric Calibration of the ACS CCD Cameras, Instrument Science Report ACS 2020-8
- Borlaff, A., Trujillo, I., Román, J., et al. 2019, A&A, 621, A133, doi: [10.1051/0004-6361/201834312](https://doi.org/10.1051/0004-6361/201834312)
- Bourque, M., & Baggett, S. 2016
- Bradley, L., Sipőcz, B., Robitaille, T., et al. 2020, astropy/photutils: 1.0.0, 1.0.0, Zenodo, doi: [10.5281/zenodo.4044744](https://doi.org/10.5281/zenodo.4044744)
- Brandt, T. D., & Draine, B. T. 2011, The Astrophysical Journal, 744, 129, doi: [10.1088/0004-637x/744/2/129](https://doi.org/10.1088/0004-637x/744/2/129)
- Caddy, S. E., Spitler, L. R., & Ellis, S. C. 2022, AJ, 164, 52, doi: [10.3847/1538-3881/ac76c2](https://doi.org/10.3847/1538-3881/ac76c2)
- Calamida, A., Bajaj, V., Mack, J., et al. 2022, arXiv
- Cambresy, L., Reach, W. T., Beichman, C. A., & Jarrett, T. H. 2001, The Astrophysical Journal, 555, 563–571, doi: [10.1086/321470](https://doi.org/10.1086/321470)
- Carleton, T., Windhorst, R. A., O’Brien, R., et al. 2022, arXiv e-prints, arXiv:2205.06347, <https://arxiv.org/abs/2205.06347>
- Cheng, Y.-T., Arai, T., Bangale, P., et al. 2021, ApJ, 919, 69, doi: [10.3847/1538-4357/ac0f5b](https://doi.org/10.3847/1538-4357/ac0f5b)
- Cohen, Y., Grogin, N. A., & Bellini, A. 2020, Space Telescope ACS Instrument Science Report
- Conselice, C. J., Wilkinson, A., Duncan, K., & Mortlock, A. 2016, The Astrophysical Journal, 830, 83, doi: [10.3847/0004-637x/830/2/83](https://doi.org/10.3847/0004-637x/830/2/83)
- Cooray, A., Bock, J. J., Keatin, B., Lange, A. E., & Matsumoto, T. 2004, ApJ, 606, 611, doi: [10.1086/383137](https://doi.org/10.1086/383137)
- Dole, H., Lagache, G., Puget, J.-L., et al. 2006, A&A, 451, 417, doi: [10.1051/0004-6361:20054446](https://doi.org/10.1051/0004-6361:20054446)
- Domínguez, A., Primack, J. R., Rosario, D. J., et al. 2011, Monthly Notices of the Royal Astronomical Society, 410, 2556–2578, doi: [10.1111/j.1365-2966.2010.17631.x](https://doi.org/10.1111/j.1365-2966.2010.17631.x)
- Dressel, L. 2012, in Wide Field Camera 3, 5
- . 2021, in WFC3 Instrument Handbook for Cycle 29 v. 13, Vol. 13, 13
- Driver, S. P. 2021, arXiv
- Driver, S. P., Andrews, S. K., Davies, L. J., et al. 2016, The Astrophysical Journal, 827, 108, doi: [10.3847/0004-637x/827/2/108](https://doi.org/10.3847/0004-637x/827/2/108)
- Dwek, E., & Arendt, R. G. 1999, AIP Conference Proceedings, 470, 354–358, doi: [10.1063/1.58621](https://doi.org/10.1063/1.58621)
- Gennaro, M. 2018, “WFC3 Data Handbook”, Version 4.0, (Baltimore: STScI)
- Giavalisco, M. 2004, Cross-Talk in the ACS WFC Detectors. II: Using GAIN=2 to Minimize the Effect, Instrument Science Report ACS 2004-13
- Giavalisco, M., Sahu, K., & Bohlin, R. C. 2002, New Estimates of the Sky Background for the HST Exposure Time Calculator, Instrument Science Report WFC3 2002-12, 9 pages
- Gilhuly, C., Merritt, A., Abraham, R., et al. 2022, ApJ, 932, 44, doi: [10.3847/1538-4357/ac6750](https://doi.org/10.3847/1538-4357/ac6750)
- Gong, Y., Cooray, A., Mitchell-Wynne, K., et al. 2016, The Astrophysical Journal, 825, 104, doi: [10.3847/0004-637x/825/2/104](https://doi.org/10.3847/0004-637x/825/2/104)
- Hauser, M. G., Arendt, R. G., Kelsall, T., et al. 1998, The Astrophysical Journal, 508, 25–43, doi: [10.1086/306379](https://doi.org/10.1086/306379)
- Hill, R., Masui, K. W., & Scott, D. 2018, Applied spectroscopy, 72, 663–688, doi: [10.1177/0003702818767133](https://doi.org/10.1177/0003702818767133)
- Hulst, H. C. v. d. 1947, The Astrophysical Journal, 105, 471, doi: [10.1086/144921](https://doi.org/10.1086/144921)
- Kashlinsky, A., Arendt, R., Gardner, J. P., Mather, J. C., & Moseley, S. H. 2004, ApJ, 608, 1, doi: [10.1086/386365](https://doi.org/10.1086/386365)

- Kawara, K., Matsuoka, Y., Sano, K., et al. 2017, Publications of the Astronomical Society of Japan, 69, doi: [10.1093/pasj/psx003](https://doi.org/10.1093/pasj/psx003)
- Kelsall, T., Weiland, J. L., Franz, B. A., et al. 1998, The Astrophysical Journal, 508, 44–73, doi: [10.1086/306380](https://doi.org/10.1086/306380)
- Kornigut, P., Kim, M. G., Arai, T., et al. 2021, arXiv
- Kornigut, P. M., Kim, M. G., Arai, T., et al. 2022, ApJ, 926, 133, doi: [10.3847/1538-4357/ac44ff](https://doi.org/10.3847/1538-4357/ac44ff)
- Koushan, S., Driver, S. P., Bellstedt, S., et al. 2021, arXiv, 503, 2033–2052, doi: [10.1093/mnras/stab540](https://doi.org/10.1093/mnras/stab540)
- Kramer, D., Carleton, T., Cohen, S. H., et al. 2022, arXiv e-prints, arXiv:2208.07218. <https://arxiv.org/abs/2208.07218>
- Lauer, T. R., Postman, M., Weaver, H. A., et al. 2021, ApJ, 906, 77, doi: [10.3847/1538-4357/abc881](https://doi.org/10.3847/1538-4357/abc881)
- Lauer, T. R., Postman, M., Spencer, J. R., et al. 2022, The Astrophysical Journal Letters, 927, L8, doi: [10.3847/2041-8213/ac573d](https://doi.org/10.3847/2041-8213/ac573d)
- Leinert, C., Bowyer, S., Haikala, L. K., et al. 1998, Astronomy and Astrophysics Supplement Series, 127, 1–99, doi: [10.1051/aas:1998105](https://doi.org/10.1051/aas:1998105)
- Li, J., Huang, S., Leauthaud, A., et al. 2022, MNRAS, 515, 5335, doi: [10.1093/mnras/stac2121](https://doi.org/10.1093/mnras/stac2121)
- Lucas, R. A., e. a. 2021
- Mack, J., Dahlen, T., Sabbi, E., & Bowers, . A. S. 2016, Space Telescope WFC3 Instrument Science Report
- Mack, J., Lucas, R., Grogin, N., Koekemoer, R. B. . A., & Koekemoer, A. 2017
- Mack, J., Olszewski, H., & Pirzkal, N. 2021, Space Telescope WFC3 Instrument Science Report
- Madau, P., & Silk, J. 2005, MNRAS, 359, L37, doi: [10.1111/j.1745-3933.2005.00031.x](https://doi.org/10.1111/j.1745-3933.2005.00031.x)
- Matsumoto, T., Tsumura, K., Matsuoka, Y., & Pyo, J. 2018, AJ, 156, 86, doi: [10.3847/1538-3881/aad0f0](https://doi.org/10.3847/1538-3881/aad0f0)
- Matsumoto, T., Matsuura, S., Murakami, H., et al. 2005, The Astrophysical Journal, 626, 31–43, doi: [10.1086/429383](https://doi.org/10.1086/429383)
- Matsumoto, T., Seo, H. J., Jeong, W.-S., et al. 2011, The Astrophysical Journal, 742, 124, doi: [10.1088/0004-637x/742/2/124](https://doi.org/10.1088/0004-637x/742/2/124)
- Matsuura, S., Arai, T., Bock, J. J., et al. 2017, The Astrophysical Journal, 839, 7, doi: [10.3847/1538-4357/aa6843](https://doi.org/10.3847/1538-4357/aa6843)
- Maurer, A., Raue, M., Kneiske, T., et al. 2012, The Astrophysical Journal, 745, 166, doi: [10.1088/0004-637x/745/2/166](https://doi.org/10.1088/0004-637x/745/2/166)
- McKay, M., & Baggett, S. 2017
- Mihos, J. C. 2019, arXiv e-prints, arXiv:1909.09456. <https://arxiv.org/abs/1909.09456>
- Robitaille, T., Sipőcz, B., Tollerud, E., et al. 2022, AstroHuntsman/gunagala: v1.0.0, v1.0.0, Zenodo, doi: [10.5281/zenodo.6796532](https://doi.org/10.5281/zenodo.6796532)
- Robotham, A. S. G., Davies, L. J. M., Driver, S. P., et al. 2018, MNRAS, 476, 3137, doi: [10.1093/mnras/sty440](https://doi.org/10.1093/mnras/sty440)
- Rowe, B. T. P., Jarvis, M., Mandelbaum, R., et al. 2015, Astronomy and Computing, 10, 121, doi: [10.1016/j.ascom.2015.02.002](https://doi.org/10.1016/j.ascom.2015.02.002)
- Rudick, C. S., Mihos, J. C., & McBride, C. K. 2011, ApJ, 732, 48, doi: [10.1088/0004-637X/732/1/48](https://doi.org/10.1088/0004-637X/732/1/48)
- Sabbi, E., & Bellini, A. 2013, Space Telescope WFC3 Instrument Science Report
- Sano, K., Matsuura, S., Yomo, K., & Takahashi, A. 2020, The Astrophysical Journal, 901, 112, doi: [10.3847/1538-4357/abad3d](https://doi.org/10.3847/1538-4357/abad3d)
- Santos, M. R., Bromm, V., & Kamionkowski, M. 2002, MNRAS, 336, 1082, doi: [10.1046/j.1365-8711.2002.05895.x](https://doi.org/10.1046/j.1365-8711.2002.05895.x)
- Schlegel, D. J., Finkbeiner, D. P., & Davis, M. 1998, The Astrophysical Journal, 500, 525–553, doi: [10.1086/305772](https://doi.org/10.1086/305772)
- Somerville, R. S., Gilmore, R. C., Primack, J. R., & Domínguez, A. 2012, Monthly Notices of the Royal Astronomical Society, 423, 1992–2015, doi: [10.1111/j.1365-2966.2012.20490.x](https://doi.org/10.1111/j.1365-2966.2012.20490.x)
- Stetson, P. B. 1987, PASP, 99, 191, doi: [10.1086/131977](https://doi.org/10.1086/131977)
- Untertorn, C. T., & Ryden, B. S. 2008, ApJ, 687, 976, doi: [10.1086/591898](https://doi.org/10.1086/591898)
- van der Wel, A., Franx, M., van Dokkum, P. G., et al. 2014, ApJ, 788, 28, doi: [10.1088/0004-637X/788/1/28](https://doi.org/10.1088/0004-637X/788/1/28)
- Windhorst, R. A., Cohen, S. H., Hathi, N. P., et al. 2011, ApJS, 193, 27, doi: [10.1088/0067-0049/193/2/27](https://doi.org/10.1088/0067-0049/193/2/27)
- Windhorst, R. A., Carleton, T., O’Brien, R., et al. 2022, AJ, 164, 141, doi: [10.3847/1538-3881/ac82af](https://doi.org/10.3847/1538-3881/ac82af)
- Wright, E. L. 1998, The Astrophysical Journal, 496, 1–8, doi: [10.1086/305345](https://doi.org/10.1086/305345)
- . 2001, The Astrophysical Journal, 553, 538–544, doi: [10.1086/320942](https://doi.org/10.1086/320942)
- Yue, B., Ferrara, A., Salvaterra, R., Xu, Y., & Chen, X. 2013, Monthly Notices of the Royal Astronomical Society, 433, 1556–1566, doi: [10.1093/mnras/stt826](https://doi.org/10.1093/mnras/stt826)
- Zemcov, M., Smidt, J., Arai, T., et al. 2014, Science, 346, 732–735, doi: [10.1126/science.1258168](https://doi.org/10.1126/science.1258168)

APPENDIX

A. SIMULATED IMAGES

In order to develop the reliable sky-SB measurements algorithms described in Section 3, we created simulated images where we know the true sky-SB and noise levels. We discuss here how these simulated images were created and the different kinds of simulated images that were produced.

We use GALSIM version 2.2.4 (Rowe et al. 2015) to generate simulated images due to its ability to generate realistic galaxies and stars easily. These simulated images include stars, galaxies, cosmic rays, and sky gradients (see Figure 11). All simulated images were produced to match WFC3/IR F125W flat-fielded images: 1014×1014 pixels, with a $0.13''$ /pixel pixel scale. Therefore, star counts, galaxy counts, PSF sizes (necessary for GALSIM) and sky levels were also based on WFC3/IR F125W data. We produced a total of 344 images with a flat sky and 444 images with a sky gradient, with exposure times from 50s to 1302s, sky-SB levels ranging from $0.22 e^-$ to $3.14 e^-$, and sky gradients ranging from a 0% change to a 20% change. We choose a wider range of sky-SB, noise, and sky gradient levels than is typical to ensure the robustness of our algorithms.

A.1. Star and galaxy counts

The star and galaxy counts for our simulated images are taken from Windhorst et al. (2011). The star count slope for WFC3/IR data, shown in Equation A1, results in nearly 1 star per 1.0 mag bin within our chosen field of view. The number of stars in each simulated image is calculated as follows:

$$N_{\text{stars},m_{\text{AB}}} = 10^{0.04(m_{\text{AB}}-18)} \quad (\text{A1})$$

where $N_{\text{stars},m_{\text{AB}}}$ is the number of stars per integer AB magnitude (m_{AB}) bin, where we assume an 18 mag bin contains exactly one star.

Stars are restricted to $18 \leq m_{\text{AB}} \leq 26$ to avoid unusually bright stars and stars below the F125W detection limit. This resulted in a total of 13 stars generated in each simulated image. Every star was generated as a Gaussian with a full width at half maximum (FWHM) of $0.136''$. The position of each star in the simulated images was randomly selected with the condition that a star's center be within the 1014×1014 grid.

The galaxy count slope is steeper at around 0.26 dex/deg. The number of galaxies in each simulated image was calculated as follows:

$$N_{\text{gal},m_{\text{AB}}} = 10^{0.26(m_{\text{AB}}-18)} \quad (\text{A2})$$

where $N_{\text{gal},m_{\text{AB}}}$ is the number of galaxies per 0.5 AB magnitude bin.

Galaxies are restricted to $18 \leq m_{\text{AB}} \leq 26.5$ to avoid unusually bright galaxies and galaxies below the F125W detection limit. This resulted in a total of 624 galaxies generated in each simulated image. Every galaxy was generated using a single-component inclined Sérsic profile (refer to Rowe et al. (2015) for profile details). Similarly to the simulated stars, the position of each galaxy in the simulated images was randomly selected with the condition that the galaxy's center be within the 1014×1014 grid.

The magnitude, effective radius, sersic index and axis ratio (b/a) were sampled using two methods: a custom distribution (described in Section A.2) and a random sampling from 3D-HST's COSMOS F125W Catalog (van der Wel et al. (2014); described in Section A.3).

A.2. Galactic Parameter Sampling Method 1: Custom Distribution

The custom galaxy sampling method is motivated by Windhorst et al. (2011). Images simulated with this method have the radius of each galaxy sampled from a distribution of the form:

$$p(R_e) = R_e \frac{e^{-R_e/0.2}}{0.2 \times \Gamma(2)} \quad (\text{A3})$$

where $p(R_e)$ is the probability density function for a galaxy with effective radius R_e , and Γ is the Gamma function. This distribution follows closely with 3D-HST COSMOS F125W galaxy counts (van der Wel et al. 2014). Due to

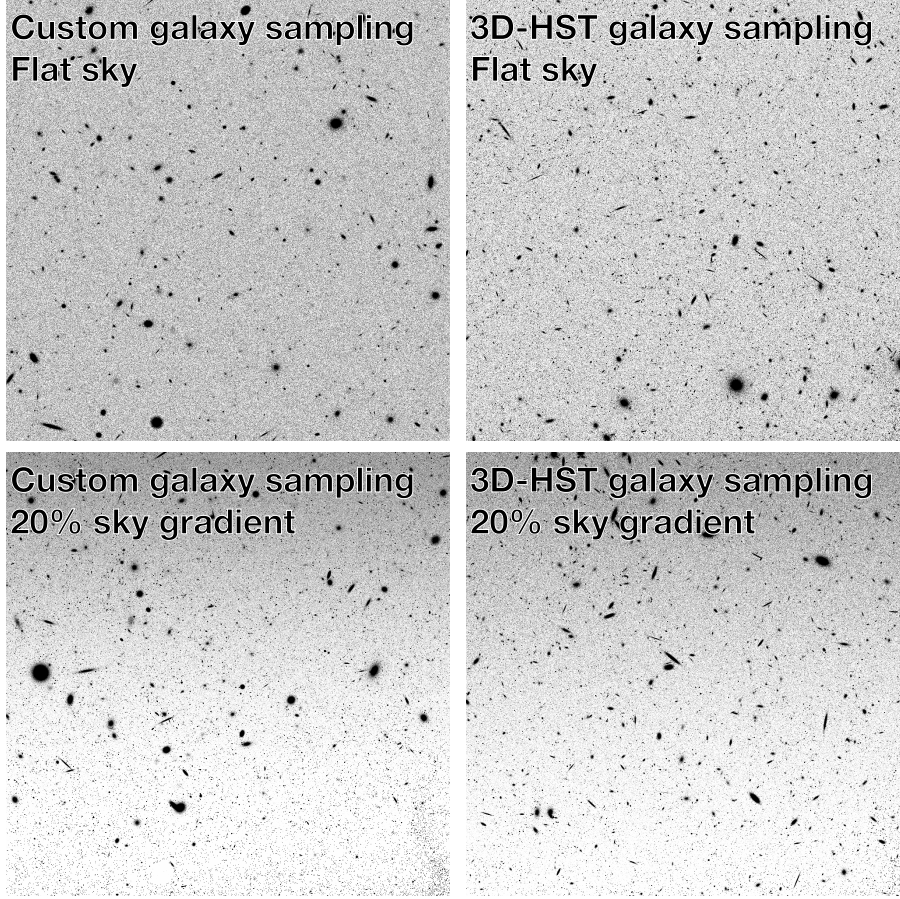


Figure 11. Example simulated images. The custom galaxy sampling method (left column) employs a distribution of galaxy parameters based on [Windhorst et al. \(2011\)](#). The COSMOS galaxy sampling method randomly selects galaxies from the COSMOS F125W database. The top images have no sky gradient added, while the bottom images have a sky gradient imposed on them.

GALSIM memory limitations, we only simulated galaxies with $R_e \leq 2.72''$. Galaxies with $R_e > 2.72''$ only account for $\ll 1\%$ of all galaxies in our field of view (follows from Equation A3).

Sérsic indices for the custom sampled galaxies follow:

$$p(n) = e^{0.38n} \quad (\text{A4})$$

where $p(n)$ is the probability density function for a galaxy with Sérsic index n . Because the allowed range of Sérsic indices for GALSIM is $0.3 \leq n \leq 6.2$, this is the range of Sérsic index values present for the galaxies in the simulated images.

AB magnitudes for the custom sampled galaxies follow:

$$p(m_{\text{AB}}) = \frac{1}{\beta} \exp\left(\frac{m_{\text{AB}} - 26.5}{\beta}\right), \quad (\text{A5})$$

where $\beta = \frac{1}{0.26 \times \ln(10)}$ and $p(m_{\text{AB}})$ is the probability density function for a galaxy with AB magnitude $18 < m_{\text{AB}} < 26.5$.

Lastly, the inclination of each galaxy produced from this method was randomly selected from the range 0 to $\frac{\pi}{2}$ radians.

A.3. Galactic Parameter Sampling Method 2: 3D-HST COSMOS F125W Catalog

Images simulated with this method used parameters directly sampled from the 3D-HST COSMOS F125W catalog (van der Wel et al. 2014). In other words, galaxies were taken directly from the 3D-HST COSMOS F125W catalog and inserted into our simulated images. Inclinations were estimated using:

$$\cos^2 i = \frac{(b/a)^2 - \alpha^2}{1 - \alpha^2} \quad (\text{A6})$$

where b/a is the axis ratio and $\alpha = 0.22$ (Untertorn & Ryden 2008).

A.4. Cosmic rays, noise and sky gradient

Cosmic rays (CRs) in the simulated images were generated by randomly selecting CRs from a WFC3/IR cosmic ray template and inserting them directly into the simulated images. The cosmic ray template was generated by identifying spikes in the individual reads of a random 1302 second HST image. This resulted in a rate of 14.6 CRs per second over the course of the exposure. The number of CRs inserted into a simulated image is given by:

$$N_{CRs} = R_{CR} \times t \quad (\text{A7})$$

where N_{CRs} is the number of cosmic rays in the simulated image, R_{CR} is the CR rate of the cosmic ray template (14.6 CR's/sec), and t is the exposure time of the simulated image.

Noise was generated for the simulated images using combination of Poisson noise and Gaussian read noise:

$$\text{RMS} = \frac{\sqrt{S_{sky} \times t + RN^2}}{t} \quad (\text{A8})$$

where S_{sky} is the sky background value, t is the exposure time, and RN is read noise. A read noise of $12 e^-$ was used for all simulated images, and various different sky-SB and exposure time values were used. Poisson noise was added to the images first, followed by Gaussian read noise.

To generate more realistic simulated images, some were modeled with linear sky gradients. These gradients were generated according to:

$$N_{row} = O_{row} + \frac{P}{100} \frac{R_{num}}{R_{tot}} O_{row} \quad (\text{A9})$$

where N_{row} are the gradient adjusted pixel values for a particular row of pixels in the image, O_{row} are the non-gradient adjusted pixel values, P is the percent change between the bottom and top row of the image, R_{num} is the row number being adjusted, and R_{tot} is the total number of rows in the image.

This method ensures that the true sky value in the gradient images is the lowest end of the gradient, aligning with our philosophy that the true sky value of a real HST image will have the least amount of light contamination and thus be the lowest sky value in an image.

B. CHOOSING THE MOST RELIABLE ALGORITHMS

Nine independent sky-SB measurement algorithms were originally created for SKYSURF, with an end goal of using the most reliable and robust methods for SKYSURF. The chosen algorithms should be able to measure the true sky-SB accurately, even for cases with sky-SB contamination. As described in Appendix A, we create simulated images with sky gradients to simulate sky-SB contamination.

The left-hand side of Figure 12 shows that there are many methods that can retrieve the true input sky-SB to less than 0.1% error. However, many of these methods (Methods 3, 4, 6, 7) assume a flat sky and can not account for sky gradients. We therefore developed several methods that account for sky gradients (Methods 1, 2, 5, 8 and 9; see right-hand plot in Figure 12). Keeping SKYSURF’s end goal of constraining an EBL signal in mind, it is crucial that we are able to robustly ignore possible sources of sky-SB contamination. These could be sky gradients in the field of view due to Earth’s limb, or the extended light profiles of galaxies. We choose the two algorithms that are able to best retrieve the known input sky-SB level from the simulated images with sky gradients: Method 2 (the Percentile-clip method) and Method 8 (the ProFound Median method).

The ProFound Median performs very well for flat images (less than 0.05% error on average). The Percentile-clip method will underestimate the sky-SB if we assume a flat sky. The median sky-SB rms for WFC3/IR F125W images in our SKYSURF database is ~ 0.05 e/s. Figure 12 shows that the Percentile-clip method can still retrieve the known input sky-SB level to within 0.3% for images with a flat sky and a sky-SB rms less than 0.05 e/s.

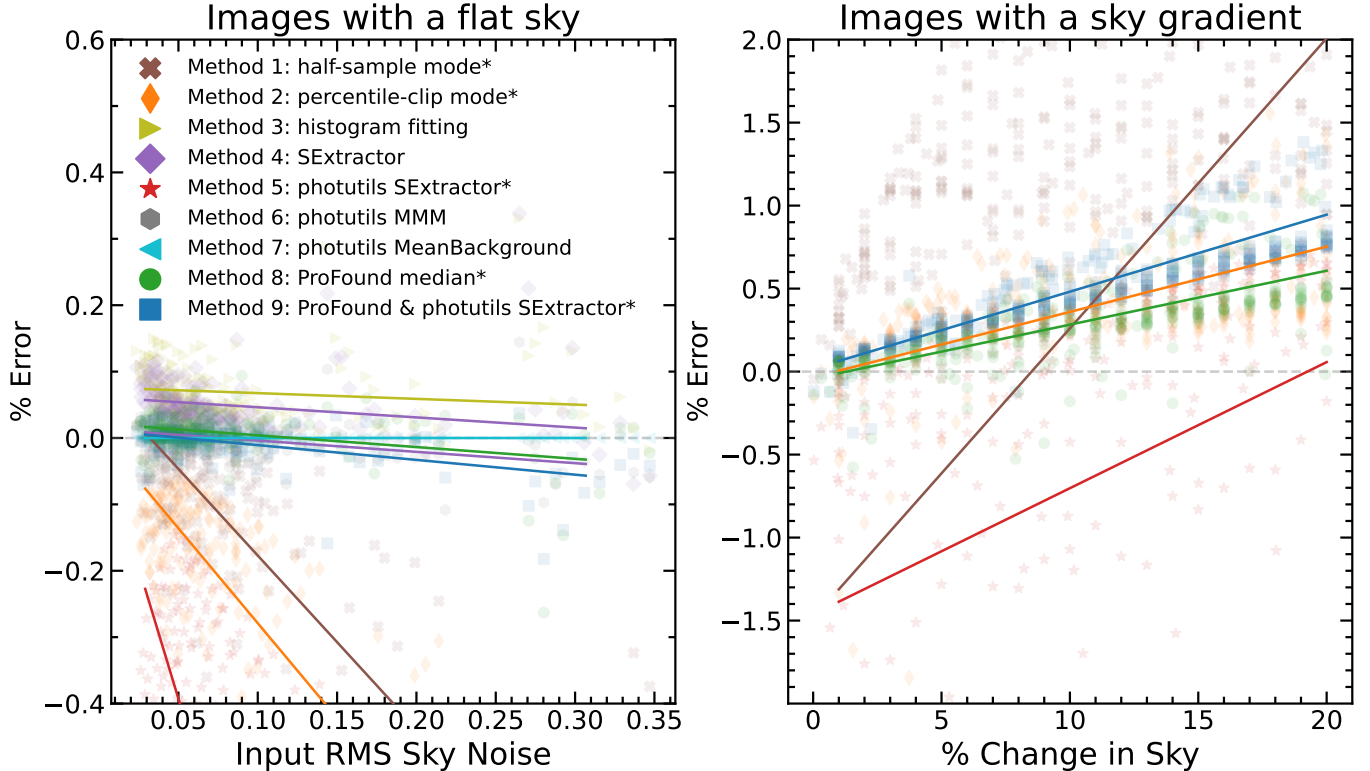


Figure 12. Results of running various sky-SB estimation algorithms (Methods 1-9) on simulated HST WFC3/IR F125W images, where $\% \text{ Error} = (\text{Measured Sky} - \text{Input Sky}) / \text{Input Sky} \times 100\%$. The solid colored lines represent the linear best fit for binned data where each bin contains 10-11 simulated images. Methods listed with an asterisk (*) are able to account for sky gradients, and are thus included in the right panel. **Left:** Algorithm performance on simulated images with no sky gradient, plotted against the known, true sky-SB rms of the simulated image. **Right:** Algorithm performance on simulated images with a sky gradient, plotted against the known sky gradient of the image.

Here we describe each method in detail as it appears on Figure 12:

Method 1: Half-sample mode - This method divides the image into 39×39 square pixel regions, then 3σ clips each sub-region. For each sub-region, it calculates the half-sample mode and rms, where the rms is determined to

be the median absolute deviation multiplied by 1.48. This is able to estimate the mode of a sample by numerically finding the smallest interval that contains half of the points in a sample and iterating until obtaining an interval with only two points (e.g., [Bickel & Fruehwirth 2005](#)). The mode of the sample is approximated to be the average of the remaining two points. This method then identifies “good” cutout regions, assuming that the true (ZL+EBL) sky-SB of an image is closest to the LPS values in an image.

Method 2: Percentile-clip - This method is described in Section 3.

Method 3: Histogram fitting - This method fits a histogram of sky-SB values from -3σ to $+1\sigma$ using a clipped sigma as a first guess, and performing 2 iterations.

Method 4: SourceExtractor - This method uses `SourceExtractor` ([Bertin & Arnouts 1996](#)) to calculate the sky-SB, where we assume that each object has a different surrounding sky.

Method 5: photutils SourceExtractor - This method masks all sources in an image then splits each image into 26×26 square pixel regions with a 30 pixel border surrounding each image that is subsequently ignored. It estimates the sky-SB value of each cutout using the `photutils SourceExtractor` algorithm ([Bradley et al. 2020](#)). The sky-SB rms is estimated using the `photutils` median absolute deviation algorithm. It rejects sub-regions with a measured sky-SB greater than the lowest sky-SB + the average sky-SB rms of all sub-regions. It also rejects sub-regions with a measured sky-SB rms greater than twice the average rms of all sub-regions. This method then estimates the sky-SB gradient of the image using the brightest 7% of cutout regions and the dimmest 7% of cutout regions. Using this calculated gradient, the algorithm determines a threshold (N) for which to include images in the final calculation, where N ranges from 4% to 35% for large to small gradients, respectively. The sky-SB of the image is the lowest N% of good cutout regions.

Method 6: photutils MMM - This method masks all the sources in the image, then calculates the sky-SB using a `photutils` method based on the DAOPHOT MMM algorithm ([Bradley et al. 2020](#); [Stetson 1987](#)).

Method 7: photutils Mean - Method 7 masks the sources in an image, 1.3σ clips the entire image, then calculates the sky-SB using `photutils MeanBackground`.

Method 8: ProFound median - This method is described in Section 3.

Method 9: ProFound & photutils Source-Extractor - This method utilizes Method 5 (`photutils SourceExtractor`) on ProFound SKY maps.

C. CROSSTALK

The charge coupled devices (CCDs) on ACS are known to suffer from crosstalk (Giavalisco 2004), where artificial “ghosts” from bright objects appear in mirror-symmetric positions in other ACS quadrants. These ghosts will appear as depressions relative to the background, with strengths of only a few electrons per pixel. However, the sky-SB itself can be on the order of a few electrons per pixel, so it is necessary we take crosstalk into consideration. Therefore, we correct for crosstalk to see how it affects our sky-SB measurements. For this simple test, we focus on ACS F775W images, where we analyze each ACS chip independently. Our default algorithm masks sky sub-regions that likely contain discrete objects. To correct for crosstalk, we reflect all masked regions to the opposite quadrant to mask the ghost corresponding to any bright objects. After reflecting masked regions, we recalculate the sky-SB level using the Per-clip method. We find that crosstalk affects the sky-SB by only 0.008% for 68% of measurements. 95% of the measurements have a 0.08% difference. We conclude that our algorithm is robust enough that crosstalk does not significantly impact sky-SB levels.

D. AMPLIFIER DIFFERENCES

The readout amplifiers can introduce additional errors to our analysis. Differences in readout noise and gain between amplifiers can cause artificial variations in the sky-SB level. Differences in sky-SB will appear as additive differences in the background for the part of the detector that is read out to a corresponding amplifier. Correcting for this without affecting the true sky-SB level is very difficult. It requires identification of differences in background level exactly at the amplifier boundaries without taking light from objects into account. This would mean only using pixels close to the amplifier boundaries, many of which are likely contaminated by discrete objects. We consider this task to be past the scope of this project. However, we test for systematic differences across our database by measuring how the mean pixel value of a pixel column varies across amplifier boundaries. The median difference between the 20 pixel columns to the left of the amplifier boundary and the 20 pixel columns to the right of the amplifier boundary is always $< 0.2\%$ for WFC3/IR images in our database. We therefore do not include amplifier differences into our uncertainty estimations.

E. TRENDS IN DARKEST SUB-REGIONS ON THE CCD

As mentioned in Section 4, if there are regions on a detector that have systematically lower sky-SB values due to flat-field error, bias error, or geometrical distortion, this could potentially bias our results. To test for systemically darker sub-regions, we create a two-dimensional histogram of the darkest sub-regions as identified using the Per-clip method (colored green in Figure 2). These sub-regions are the darkest 5% of all sub-regions in an image. We refer to these as the “darkest sub-regions” for this discussion.

The resulting histograms are shown in Figures 13-15. Bluer boxes indicate regions where most SKYSURF images contain a darkest sub-region in the corresponding location on the detector. In other words, bluer regions are systematically darker. Redder boxes indicate regions where most SKYSURF images do not contain a darkest subregion in the corresponding location on the chip. For ACS/WFC and WFC3/UVIS, there is a clear structure in the histograms that resemble the flat-fields (Mack et al. 2017; Dressel 2021). The structure for WFC3/IR is less obvious, where the darkest sub-regions instead tend along the WFC3/IR amplifier boundaries.

We test how these systematically darker/ brighter sub-regions affect our sky-SB measurements. Because Figures 13-14 resemble flat fields, we use this test to quantify uncertainties in flat field estimates. We use the histograms in Figures 13-15 to find the systematically darkest (darkest 5% of sub-regions) and brightest regions (brightest 5% of sub-regions). For every SKYSURF image in a filter, we take the mean sky-SB of the previously identified darkest regions and the mean sky-SB of the brightest regions. Note that these regions are the *same* for every image in a filter because they are determined using Figures 13-15.

We can compare the mean of the darkest and brightest regions to estimate the maximum level of uncertainty that the structure seen in Figures 13-15 add to our sky-SB levels. We only use images that have reliable sky-SB levels (Section 5). Figure 16 shows the ratio of the brightest and dimmest sub-regions. We find that WFC3/IR does not show significant sky-SB differences between the darkest and brightest regions. However, WFC3/UVIS and ACS/WFC tend to show $\sim 2 - 5\%$ differences.

This test gives a maximum possible flat-field uncertainty on aperture photometry. We still adopt Mack et al. (2016) as our flat field uncertainty for SKYSURF sky-SB measurements.

ACS/WFC

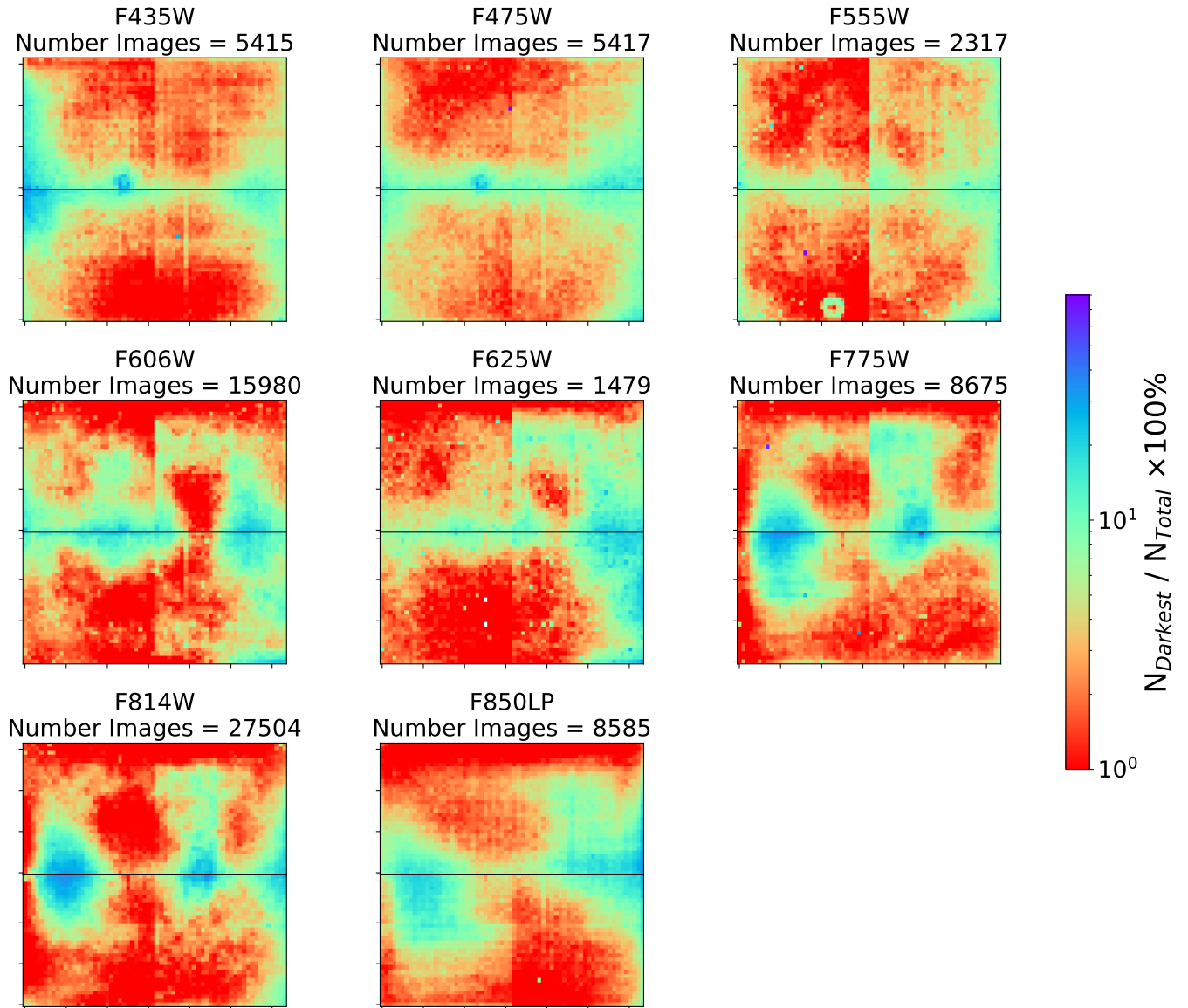


Figure 13. Two-dimensional histograms of the darkest sub-regions (or the green sub-regions shown in Figure 2) for all the images in every filter in ACS/WFC. The colorbar indicates the percent of images ($N_{\text{Darkest}}/N_{\text{Total}} \times 100\%$ where N_{Darkest} is the number of darkest sub-regions and N_{Total} is the total number of images) in this filter that contain a darkest sub-region in the corresponding location. In other words, regions that are more blue/ purple have systematically lower sky-SB levels across the entire filter.

WFC3/UVIS

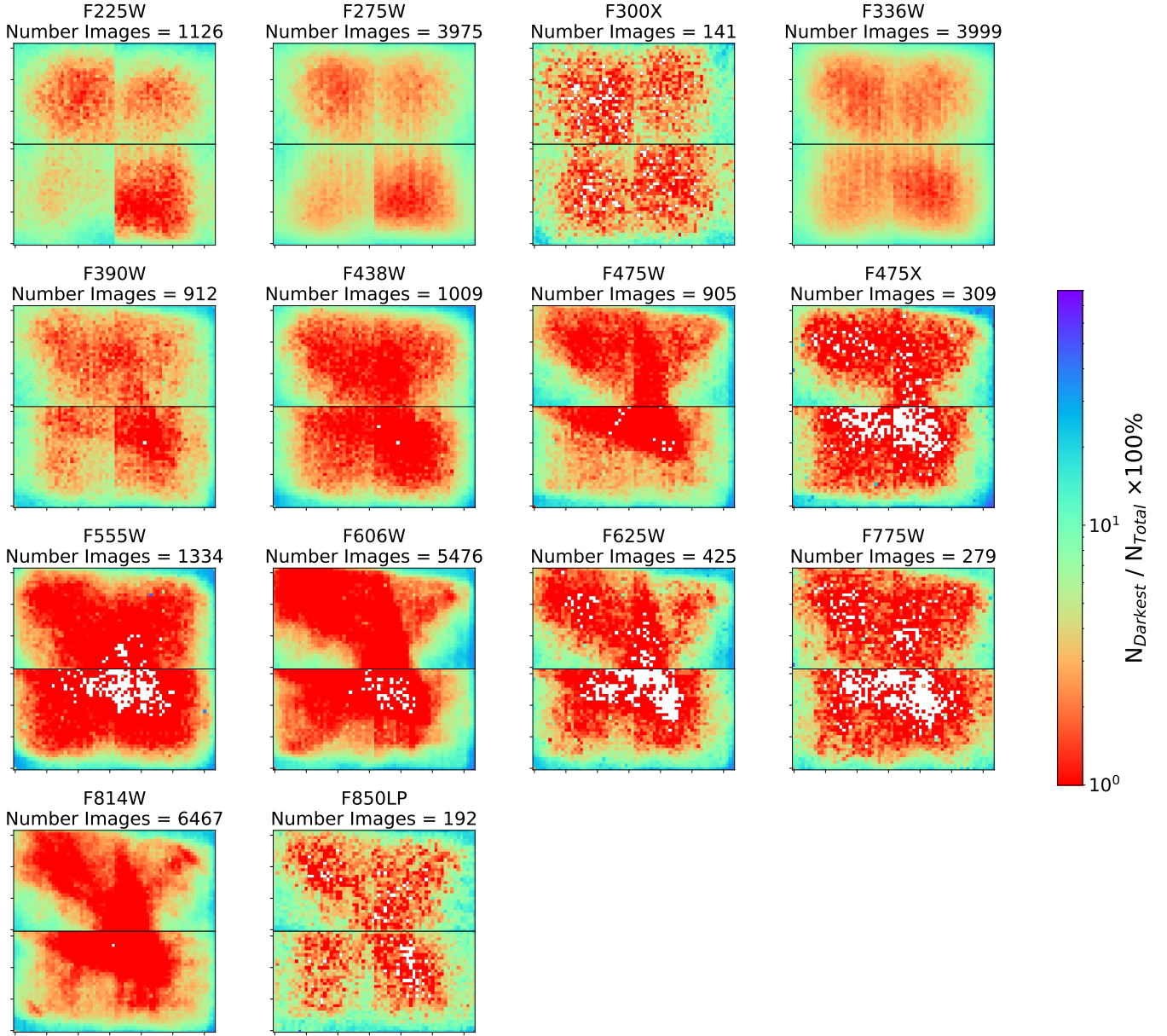


Figure 14. Two-dimensional histograms of the darkest sub-regions (or the green sub-regions shown in Figure 2) for all the images in every filter in WFC3/UVIS. The colorbar indicates the percent of images ($N_{\text{Darkest}}/N_{\text{Total}} \times 100\%$ where N_{Darkest} is the number of darkest sub-regions and N_{Total} is the total number of images) in this filter that contain a darkest sub-region in the corresponding location. In other words, regions that are more blue/ purple have systematically lower sky-SB levels across the entire filter. White indicates regions that are always ignored due to detector artifacts or regions that always contain a bright object.

WFC3/IR

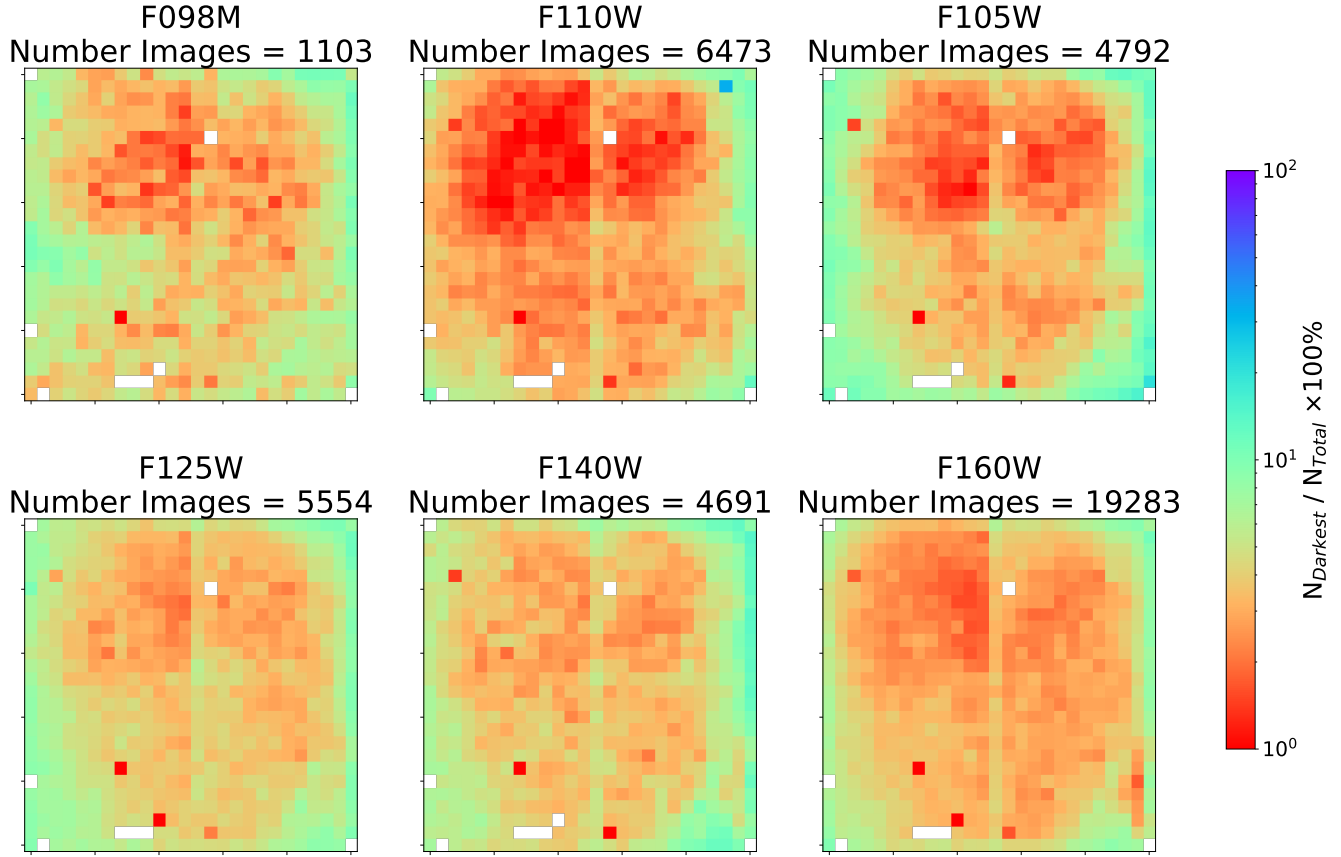


Figure 15. Two-dimensional histograms of the darkest sub-regions (or the green sub-regions shown in Figure 2) for all the images in every filter in WFC3/IR. The colorbar indicates the percent of images ($N_{\text{Darkest}}/N_{\text{Total}} \times 100\%$ where N_{Darkest} is the number of darkest sub-regions and N_{Total} is the total number of images) in this filter that contain a darkest sub-region in the corresponding location. In other words, regions that are more blue/ purple have systematically lower sky-SB levels across the entire filter. White indicates regions that are always ignored due to detector artifacts. Known artifacts that are always masked are the “death star” (bottom middle) and “wagon wheel” (bottom right corner)

Comparing Systematically Brightest and Darkest Sub-regions

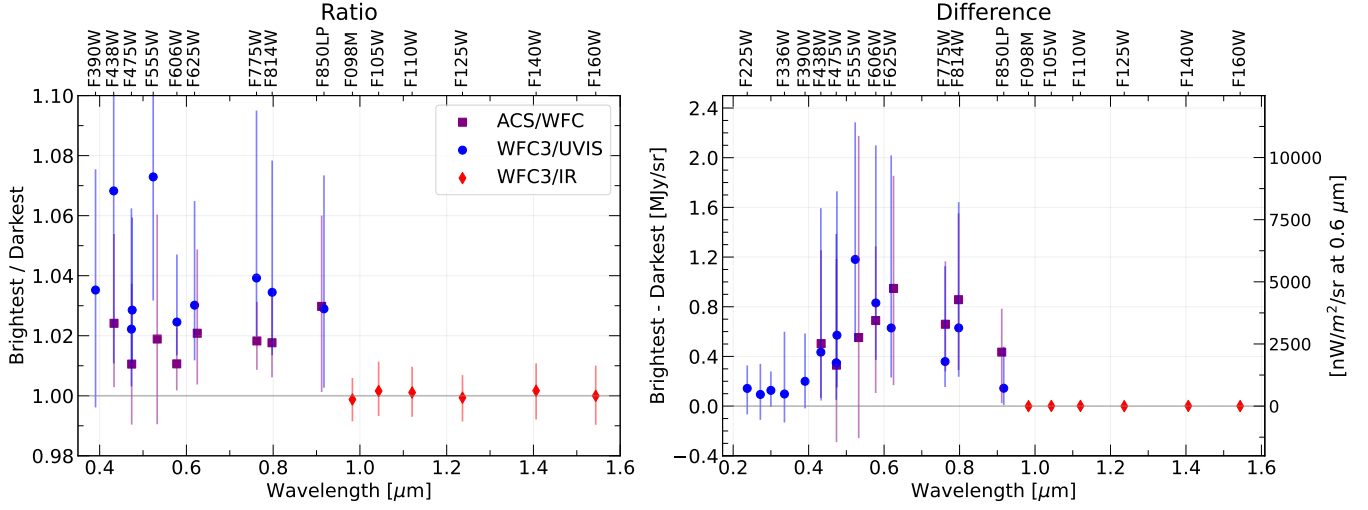


Figure 16. Comparison of the systematically brightest and darkest sub-regions (using the Per-clip method). The error bars for both plots show the 16th- and 84th-percentiles of the y-axis distribution. **Left:** Median ratio of the brightest sub-regions over the darkest sub-regions. The 84th-percentile limits are cut off for F438W (1.37) and F555W (1.14) to better display the other filters. The bluest filters are excluded because the sky-SB is nearly zero. The average ratio for WFC3/UVIS is 1.05 and the average ratio for ACS/WFC is 1.02. **Right:** Median difference of the brightest sub-regions over the darkest sub-regions. The left y-axis shows units of MJy sr^{-1} and the right axis shows $\text{nW m}^{-2} \text{sr}^{-1}$ at $0.6 \mu\text{m}$.

F. WFC3/UVIS DETECTOR DIFFERENCES

The two WFC3/UVIS detectors were carved from different wafers, and differences in the properties of these detectors could affect sky-SB estimations (as mentioned in Section 4). Additionally, if certain apertures are more commonly used, this could cause one detector to have a higher average sky-SB. To ensure these differences do not influence our sky-SB results, we compare differences in sky-SB between the UVIS1 and UVIS2 detectors. As highlighted in Figure 17, we find almost no differences in the sky-SB levels between both detectors. The differences are typically $\leq 1\%$. The UV filters are excluded from the left plot because the sky-SB is close to zero. We confirm that these differences are still typically $\leq 1\%$ when using the Pro-med algorithm.

To ensure we only use the most reliable sky-SB measurements for this test, we also exclude images with high exposure times or images where one chip has significantly more flagged regions than the other chip. Higher exposure times (which we define as > 2400 sec) require that HST be operating for a greater portion of the orbit, meaning it is close to the Earth's limb for a proportionally longer amount of time. This can cause sky gradients that could cause one detector to be brighter than the other. We exclude images where the number of good regions is not within 100 regions (or $\sim 5\%$ of total regions) to each chip in case one chip systematically contains more bright objects than the other.

Comparing WFC3/UVIS Chips

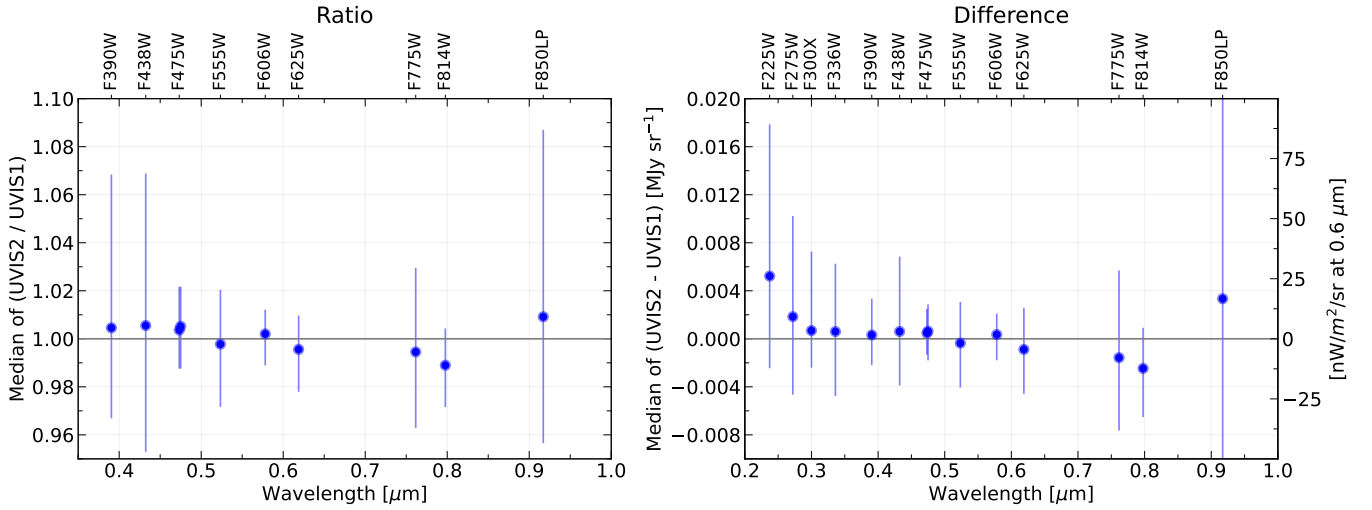


Figure 17. Comparison of sky-SB measurements (using the Per-clip Method) between both detectors for WFC3/UVIS. Each point only includes reliable images, and represents the median chip difference for that filter. The error bars show the 16th- and 84th-percentiles of the y-axis distributions. **Left:** Median ratio of the UVIS2 sky-SB over the UVIS1 sky-SB. The bluest filters are excluded because the sky-SB is nearly zero. **Right:** Median difference of the UVIS2 sky-SB minus the UVIS1 sky-SB. The left y-axis shows units of MJy sr^{-1} and the right axis shows $\text{nW m}^{-2} \text{sr}^{-1}$ at $0.6 \mu\text{m}$.

G. CONVERTING TO FLUX UNITS

Given the confusion that sometimes arises on this topic, in this section we explain our methods to convert our sky-SB measurements to units of spectral flux density. The conversions for each camera are highlighted in Equations G10-G12. We use pixel areas of $0.135 \times 0.121 \text{ arcsec}^2$ for WFC3/IR, $0.0395 \times 0.0395 \text{ arcsec}^2$ for WFC3/UVIS and $0.050 \times 0.050 \text{ arcsec}^2$ for ACS/WFC.

$$I_{\lambda, \text{WFC3/IR}} = \frac{S_{\text{chip}} \times \text{PHOTFNU}}{A} \quad (\text{G10})$$

$$I_{\lambda, \text{WFC3/UVIS}} = \frac{S_{\text{chip}} \times \text{PHTFLAM}(\text{converted})}{A} \quad (\text{G11})$$

$$I_{\lambda, \text{ACS/WFC}} = \frac{S_{\text{chip}} \times \text{PHTFLAM}(\text{converted})}{A} \quad (\text{G12})$$

For WFC3/IR in Equation G10, S_{chip} is the measured sky-SB in units of electrons per second (e^-/s), PHOTFNU is the inverse sensitivity taken from the image header in units of $\text{Jy}/(e^-/s)$, and A is the average pixel area in units of steradians. When using SKYSURF sky-SB measurements for SKYSURF, a thermal dark signal must be subtracted (Carleton et al. 2022). Please refer to Carleton et al. (2022) for updated estimates on thermal dark levels.

For WFC3/UVIS and ACS/WFC, we use the chip-dependent inverse sensitivity from the image header (PHTFLAM), which is originally in units of $\text{erg cm}^{-2} \text{ \AA}^{-1} \text{ s}^{-1}$, and convert it to units of Jy (PHTFLAM(converted)) using the chip-dependent pivot wavelength listed in the header (PHTPLAM). This conversion is done using `astropy.units` (Astropy Collaboration et al. 2013, 2018).

H. TRENDS IN SKY-SB RMS

We show the median measured sky-SB rms for each filter in Figure 18. The trends seen here closely match trends seen in Figure 3 and Figure 4. WFC3/IR shows lower measured sky-SB rms values likely due to the larger pixel size (see pixel sizes described in Appendix G).

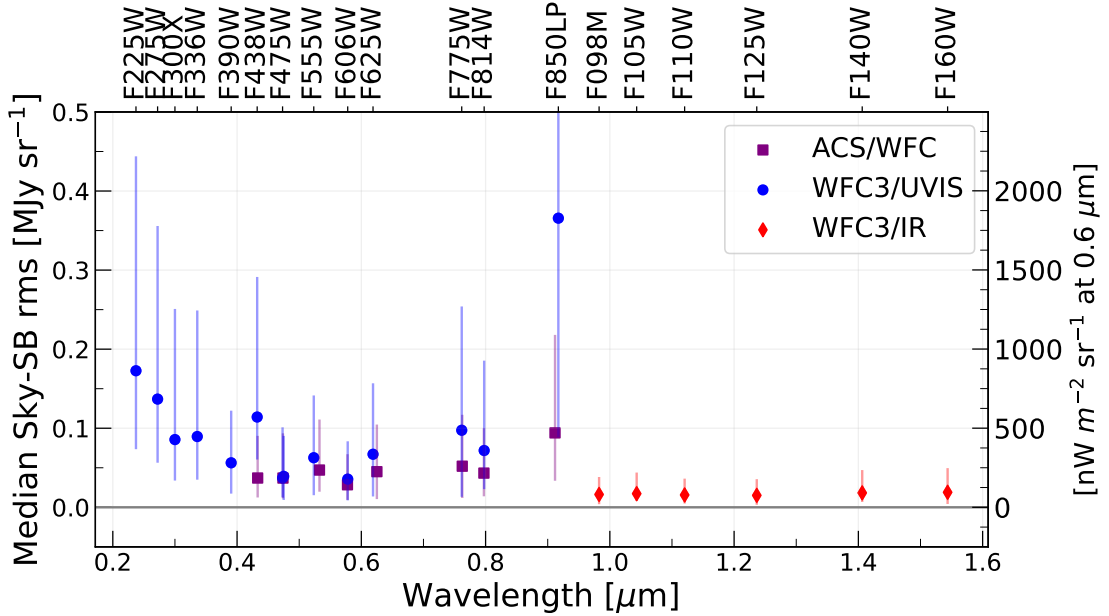


Figure 18. Median sky-SB rms for each filter. The error bars show the 16th- and 84th-percentiles of the rms distributions.

I. TESTING HOW DIFFERENT CTE CORRECTIONS AFFECT THE WFC3/UVIS SKY-SB

As described in Appendix B.2 of [SKYSURF-1](#), we redownloaded WFC3/UVIS images calibrated with the newest `calwf3` version at the time: `calwf3 v3.6.0`. This version of the standard calibration pipeline presents updates to the CTE corrections. Since CTE corrections adjust pixels containing a sky-SB signal, we ensure these updated corrections do not significantly affect sky-SB measurements. Results are shown in Table 5. The sky-SB rms improves for all filters, with sky-SB rms values typically being 2–5% lower with the v3.6.0 corrections. We find an average median offset in sky-SB between both pipelines of $\sim 0.007\%$ for filters longward of $0.4 \mu\text{m}$ and an average median offset between both pipelines of $\sim 1.9\%$ for filters shortward $0.4 \mu\text{m}$.

Filter	Median Sky Ratio	Median Sky rms Ratio
F225W	0.979750	0.978251
F275W	0.877970	0.969360
F300X	1.037716	0.952036
F336W	1.014963	0.979252
F390W	0.997349	0.975110
F438W	1.002838	0.975508
F475X	1.008633	0.964548
F475W	1.000642	0.969892
F555W	0.999497	0.970605
F606W	1.001499	0.958634
F625W	0.999005	0.962439
F775W	0.987096	0.973376
F850LP	0.999113	0.972571
F814W	1.001019	0.963322

Table 5. Median ratio of the `calwf3 v3.5.0` / `calwf3 v3.6.0` sky-SB values and sky-SB rms values. Only reliable sky-SB measurements are used in this comparison.

J. SUN ANGLE MODEL COMPARISON

Following the discussion from Section 6, we test how current models can replicate our measured sky-SB as a function of Sun Angle. Specifically, we compare our measurements to the Zodiacal model from [Aldering \(2001\)](#), using the `gunagala` ([Robitaille et al. 2022](#)) sky module. For every SKYSURF image, we use the time and coordinates of the observation to predict ZL emission. We plot these as grey points in Figure 19 for 3 example filters. SKYSURF sky-SB measurements are shown as black crosses, which represent the median sky-SB for each 30 deg Sun Angle bin. We show results for a low Ecliptic latitude range and a higher latitude range. Figure 19 shows that our measurements in general agree with the [Aldering \(2001\)](#) Zodiacal model. The most major offsets are seen at redder wavelengths, where the shape of the sky-SB as a function of Sun Angle does not follow the model.

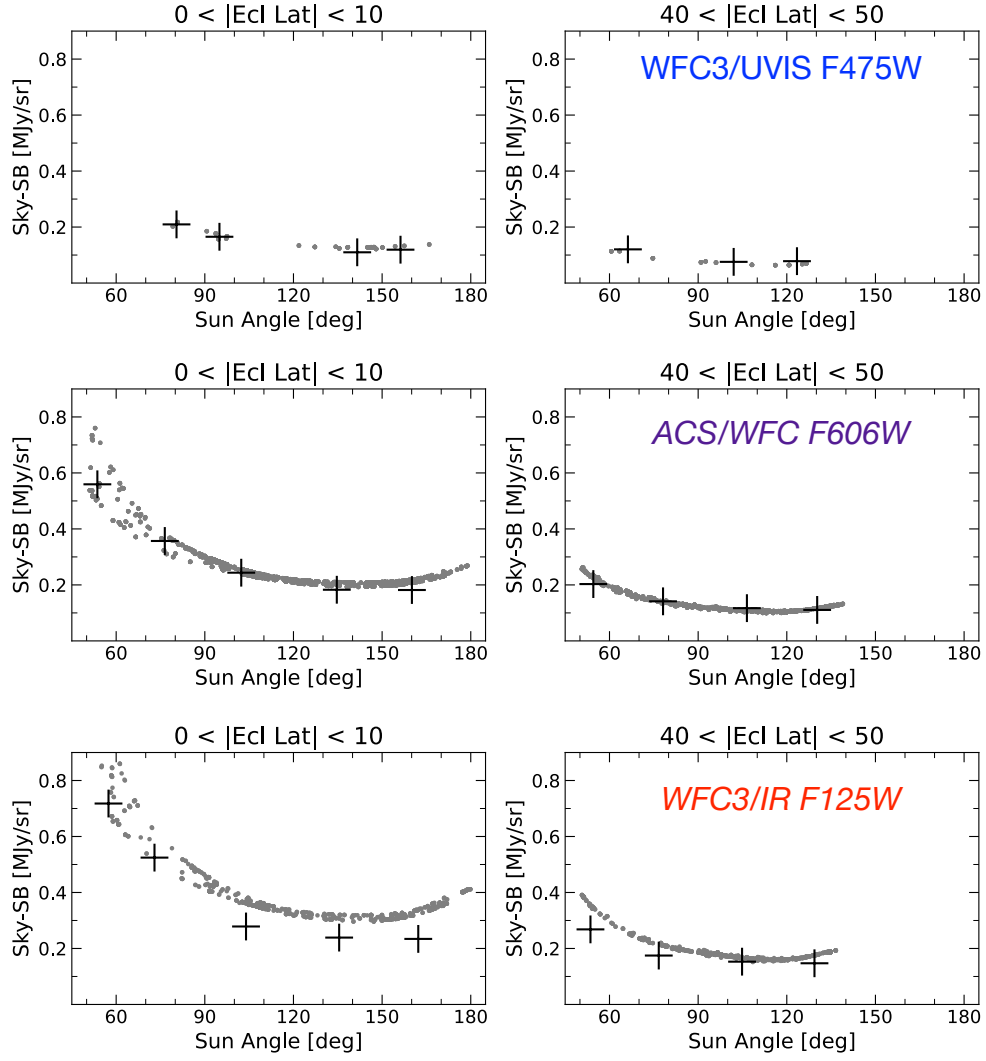


Figure 19. Comparison of SKYSURF sky-SB measurements and ZL emission predictions as a function of Sun Angle. Grey points show Aldering (2001) predictions for Zodiacal emission for every SKYSURF image. The black crosses show median SKYSURF sky-SB measurements for every 30 deg Sun Angle bin.

K. ENSURING A RELIABLE DIFFUSE LIGHT ESTIMATE

We ensure our methods described in Section 7 result in a reliable Diffuse Light estimate. Figure 20 shows a one-to-one plot of sky-SB measurements used in *SKYSURF-2* and those presented in this work. There are no noticeable trends in Figure 20, meaning that at first order, taking a median difference between *SKYSURF-2* and this work will result in consistent results, whether or not we utilize the darkest or the brightest sky-SB values.

SKYSURF-2 uses the Lowest Fitted Sky (LFS) method to estimate the DL, which utilizes the darkest sky-SB measurements. To ensure our calculated sky-SB difference represents the darkest sky-SB values necessary for the LFS method, we plot the difference in sky-SB (This Work – *SKYSURF-2*) as a function of the sky-SB measured in *SKYSURF-2*. The red lines show the median difference used to estimate DL in Table 4. The red lines agree with the darkest sky-SB measurements, confirming that the method to estimate DL limits in this work is consistent with the LFS method from *SKYSURF-2*.

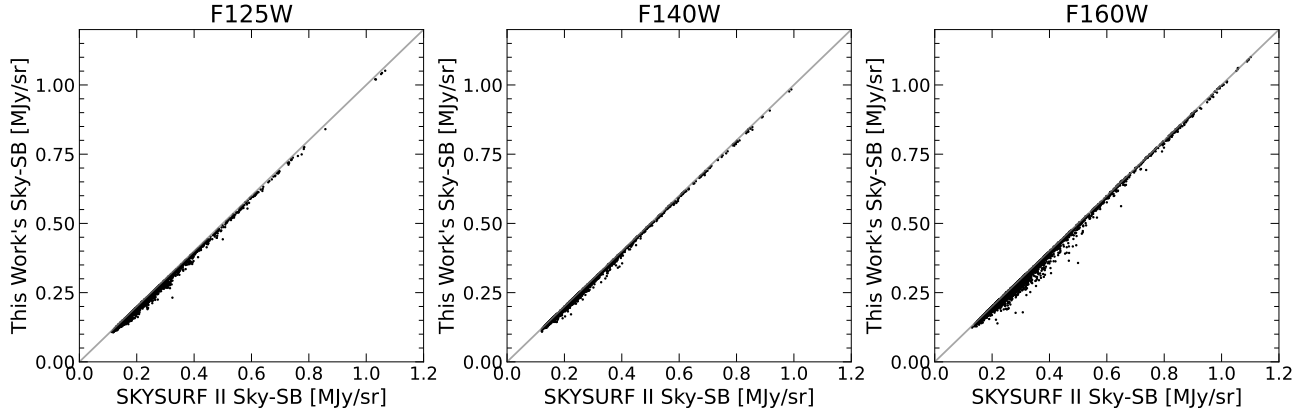


Figure 20. One-to-one relationship of the sky-SB measurements in this work (using the Per-clip algorithm) and the measurements in *SKYSURF-2*. The x-axis shows sky-SB measurements from *SKYSURF-2* and the y-axis shows sky-SB measurements from this work. The grey line is a one-to-one relationship.

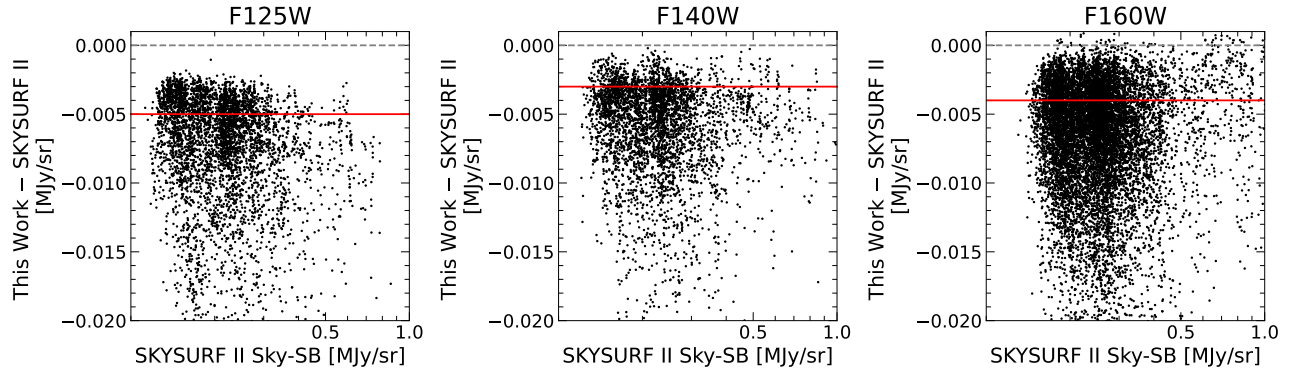


Figure 21. Relationship of the sky-SB measurements in this work (using the Per-clip algorithm) and the measurements in *SKYSURF-2*. The x-axis shows sky-SB measurements from *SKYSURF-2* and the y-axis shows the difference in sky-SB values between this work and *SKYSURF-2*. The red lines indicate the median differences shown in Table 4 used for DL estimations. The red lines agree with the darkest sky-SB measurements from *SKYSURF-2*.